THESIS FOR THE DEGREE OF DOCTOR OF PHILOSOPHY

The self-spreading double bilayer

Advances in lipid membrane nanotechnology

IREP GÖZEN

Department of Chemical and Biological Engineering

CHALMERS UNIVERSITY OF TECHNOLOGY

Göteborg, Sweden 2013

The self-spreading double bilayer

Advances in lipid membrane nanotechnology

IREP GÖZEN

Department of Chemical and Biological Engineering

Chalmers University of Technology

SE-412 96 Göteborg

Sweden

Telephone + 46 (0)31-772 1000

Cover: Rupture Morphologies in Phospholipid Membranes

"Electrify"	*"Valentine"*	*"Ascent"*	*"Creep"*
"Touch"	*"Crystal"*	*"Join"*	*"Freeze"*
"Tin Tin"	*"Nova"*	*"Flame"*	*"Kiss"*

Backcover photo by Peter Sandin.

The self-spreading double bilayer

Advances in lipid membrane nanotechnology

IREP GÖZEN

Department of Chemical and Biological Engineering

Chalmers University of Technology

ABSTRACT

In my thesis I describe the generation, characterization and uses of self-spreading double bilayers. This new type of solid-supported model membrane combines features and properties of the 2D lipid bilayer membrane, and the 3D phospholiposome. The double bilayer membrane, i.e., a fully closed, parallel stack of two lipid bilayers, is essentially a surface-adhered flat giant unilamellar vesicle (FGUV) with a very small internal volume. It possesses features of supported membranes, such as flatness, large area coverage and high mechanical stability, and of giant vesicles, such as the ability to encapsulate nanoparticles in its interior volume. In the experimental work towards this thesis, I have probed the response of the FGUV to chemical or physical cues, and studied dynamic features reminiscent of complex cell behavior. A number of examples are discussed, including protrusion formation as a response to a chemical gradient, directed and reversible movement in a temperature gradient, spontaneous nanotube formation in response to the adhesion of virus-like particles, and repair of large area membrane pores. An important outcome of my work is the discovery of two non-trivial pore formation modes in membranes, which links biomembrane materials properties to fundamental properties of thin solid materials. One of the modes displays crackling noise dynamics, featuring sudden intermittent bursts over a broad size range (avalanches), similar to earthquakes. I consider the FGUV to be an experimental model system for studying various aspects of cell like behavior on intact model membranes, as well as a nanotechnological platform, useful to construct mesoscale membrane architectures and networks.

Keywords: lipid double bilayer, rupture, pore, self-spreading, tension, nanotechnology, vesicle, flat giant unilamellar vesicle, crackling noise, viscous fingering

LIST OF PUBLICATIONS

Paper **I**. T. Lobovkina, I. Gözen, Y. Erkan, J. Olofsson, S. G. Weber and O. Orwar
Protrusive Growth and Periodic Contractile Motion in Surface Adhered Vesicles induced by Ca²⁺ gradients.
Soft Matter, 2010, 6, 268 - 272.

Paper **II.** I. Gözen, M. Shaali, A. Ainla, B. Örtmen, I. Põldsalu, Kiryl Kustanovich, Gavin Jeffries, Z. Konkoli, P. Dommersnes and A. Jesorka
Thermal Migration of Molecular Lipid Films as Contactless Fabrication Strategy for Lipid Nanotube Networks. Submitted Manuscript.

Paper **III**. I. Gözen, C. Billerit, P. Dommersnes, A. Jesorka and O. Orwar
Calcium-Ion-Controlled Nanoparticle-Induced Tubulation in Supported Flat Phospholipid Vesicles.
Soft Matter, 2011, 7, 9706 - 9713.

Paper **IV**. I. Gözen, P. Dommersnes, I. Czolkos, A. Jesorka, T. Lobovkina and O. Orwar
Fractal Avalanche Ruptures in Biological Membranes.
Nature Materials, 2010, 9, 908 - 912.

Paper **V**. I. Gözen, P. Dommersnes, O. Orwar, A. Jesorka
Evidence for Membrane Flow through Pores in Stacked Phospholipid Membranes.
Soft Matter, 2012, 8, 6220.

Paper **VI**. I. Gözen, B. Ortmen, I. Põldsalu, P. Dommersnes, O. Orwar, A. Jesorka
Repair of Large Area Pores in Solid Supported Bilayers.
Soft Matter, 2013, In Press (DOI: 10.1039/c3sm27429b).

Paper **VII**. A. Ainla, I. Gözen, O. Orwar and A. Jesorka
A Microfluidic Diluter Based on Pulse Width Flow Modulation.
Anal. Chem., 2009, 81, 5549 - 5556.

Paper **VIII**. A. Ainla, I. Gözen, B. Hakonen and A. Jesorka
Lab on a Membrane: a Toolbox for Reconfigurable 2D fluidic networks. Submitted Manuscript.

List of related peer-reviewed publications by the author that are not included in this thesis:

I. Gözen and A. Jesorka
Instrumental Methods to Characterize Molecular Phospholipid Films on Solid Supports.
(Review), Anal. Chem., 2012, 84 (2), 822–838.

I. Gözen, P. Roux, C. Billerit, P. Dommersnes, O. Orwar and A. Jesorka
Nanoparticle induced multi-vesiculation of phospholipid tubes. Proceedings of 2nd International Workshop on Complex Physical Phenomena in Materials (2012, Brazil) ISBN: 978-82-93224-07-5.

CONTRIBUTION REPORT

Paper **I**.   Designed and performed some of the experiments and performed the spreading growth analysis.

Paper **II**.   Designed and performed all thermomigration experiments, wrote most of the manuscript.

Paper **III**.   Designed and performed the majority of the experiments, performed the analysis, wrote most of the manuscript.

Paper **IV**.   Designed and performed all experiments. Equally contributed to the writing of the manuscript with P. Dommersnes.

Paper **V.**   Designed and performed all experiments, performed the analysis, wrote most of the manuscript.

Paper **VI.**   Designed and performed all experiments, performed the analysis, wrote most of the manuscript.

Paper **VII**.   Designed and performed some of the lipid film experiments. Contributed to the writing of the experimental part of the manuscript.

Paper **VIII**.   Designed and performed some of the lipid film experiments. Contributed to the writing of the experimental part of the manuscript.

CONTENTS

Chapter 1 : INTRODUCTION

The inherent complexity of the biological cell is still poorly understood. Complexity emerges if a system, such as the cell[1], is composed of a large number of interactive components, and exhibits properties which are not apparent from the properties of the individual parts. Biological membranes organize cellular complexity, and thus establish and promote structure in the living world[2]. The responsibilities of membranes are many, for example they compartmentalize the cell, form transport networks, organize proteins and serve as a smart barrier for molecules and ions. The fundamental structure of the cell membrane is the phospholipid bilayer, consisting of a large number of individual phospholipid molecules, which organize themselves spontaneously in a self-assembly process[3-4]. The membrane has peculiar characteristics, it is highly dynamic and features two-dimensional fluidity[5], and it can accommodate proteins and other functional molecules. From early on, the dynamic features in combination with the relatively simple fabrication by a self-assembly process, which worked also well in vitro, made lipid bilayers interesting model systems for the cell membrane[6]. Moreover, due to their tendency to form spherical compartments, which under appropriately chosen fabrication conditions are similar in size to the living cell, cell-like containers, or "protocells", can be created[7-10]. This provides plenty of opportunity for experimental exploration of selected structural or functional aspects derived from the biological antetype. This constructive, bottom-up approach to understanding cellular complexity has grown into a research field of its own. Naturally, lipid membrane-based model cells are simpler than the biological original, but can be continuously improved and extended if required, approaching more sophisticated architectures with abilities such as compartment formation[11], migration towards a stimulus[12], control of chemical reactions such as enzymatically catalyzed transformations and self-replication[13-14]. In contrast, the top-down approach involves typically the genetic reprogramming of an existing cell. Here, the starting point is a living cell and by knocking out specific genes, minimalistic

cell models are created, which carry only an essential genome that can maintain basic metabolic functions[15].

The goal of my thesis work was the development and investigation of a new type of model membrane, which combines features and properties typical for the two-dimensional supported lipid bilayer membrane, and the three dimensional phospholiposome, or vesicle. This "supported double bilayer membrane", i.e., a closed parallel stack of two lipid bilayer membranes, is essentially a surface-adhered flat giant unilamellar vesicle (FGUV) with a very small internal volume. The water layer encapsulated by the FGUV is only a few tens of nanometers thick, meaning that a 100 µm vesicle with a 10 nm inter-bilayer space has a volume of about 750 fL. On one hand, the transport and exchange conditions in a cell compartment would be much more realistically represented by such confined volume, than by a giant vesicle of the same diameter. On the other hand, the fluidic properties of the proximal (lower) and distal (upper) bilayer are very different. The distal bilayer is not only more fluid than the adhered proximal bilayer, it can also be seen as a special kind of cushioned bilayer, potentially supporting the incorporation of fully functional membrane proteins. Thus, the FGUV is a promising nanotechnological platform, which can serve both as model membrane and as protocell or cell compartment. It adds new possibilities to the current range of biomimetic membrane applications, which is populated by supported monolayers, bilayers and tethered bilayers.

The FGUV is produced by self-spreading of lipid membrane from a multilamellar (or onion shell) lipid vesicle (MLV) which is brought in contact with the surface support, typically a metal oxide or a semi-metal oxide surface. The FGUV is at all times connected to the MLV, the tension changes in the vesicle can therefore be compensated by the reservoir, similar to wrinkles in red blood cells or lipid droplets in eukaryotic cells[16-17]. Once an FGUV is formed on the substrate, its growth can be induced or stopped, simply by changing the ionic content. The supported double bilayer is a robust structure, and easily accessible by instrumental methods. Manipulation and stimulation are easily achieved by various means, including microinjection needles, local heating techniques, and microfluidic tools. In my experimental work, I have probed the response of the FGUV to chemical or physical cues, and captured dynamic features reminiscent of complex cell behavior. Examples discussed in the text, and presented as original research publications, are protrusion formation in response to chemical gradients, directed and reversible movement in a temperature

gradient, spontaneous nanotube formation as a response to the adhesion of virus-like particles, and repair of membrane pores. One of the most important outcomes of my work is the discovery of two non-trivial rupture modes in biological membranes, which links biomembrane materials properties to fundamental properties of thin solid state materials.

In chapter 2 I explain the concept of surface energy, surface tension, interfaces and the wetting phenomenon. Wetting of surfaces by lipids can be seen as the basis for the FGUV formation on solid supports.

In chapter 3 I introduce the biophysics of lipid membranes in greater detail. The interpretation of the phenomena observed and reported in this work benefits from a detailed understanding of the underlying chemical and physical aspects.

In chapter 4 I discuss the two newly discovered rupture modes and their relation to flow in porous media. One of these two rupturing modes, fractal ruptures, connects the properties of solid state materials with fluid membranes.

In chapter 5, I provide background on the artificial cell concept, as one of the motivations behind my work. I present current approaches in artificial cell research and address the aspects connected to my work.

In chapter 6, I describe in a nutshell the methods used in the experiments, including light microscopy imaging, fabrication and characterization of surfaces, and microfluidic technology.

In the final chapter the published and submitted papers are summarized.

Chapter 2 : SURFACES, INTERFACES and WETTING PHENOMENA

2.1 Surface free energy

Solid surfaces are an important aspect of the work presented in this thesis. Supported lipid membranes are fabricated on surfaces, and many of the membrane properties depend on the surface properties, such as surface charge, material or roughness. The wetting phenomenon observed in double bilayers only occurs on solid high energy surfaces, for example SiO_2 or Al_2O_3 films. In the following section I will briefly explain why surfaces have energy and why they can be categorized as high or low energy surfaces.

The reason for surface energy lies in the interactions between the individual molecules within that surface. If the attraction of a group of molecules to each other is stronger than thermal agitation, those molecules transform from the gas to the liquid phase, a denser although still disordered, condensed state in which the molecules attract one another[18]. For that reason, a molecule in the bulk of a liquid experiences favorable cohesive interactions with its neighboring molecules; while by contrast a molecule at the surface of the liquid experiences disrupted unsatisfied cohesive interactions (**Figure 2.1 A**). As a result surface atoms possess energy which they tend to reduce. This energy is called surface free energy or surface tension [18-19].

The creation of a unit area with an unsatisfied cohesive layer of atoms can be visualized as the separation of a block of solid material into two pieces with a half unit area each (**Figure 2.1 B**). In this case molecular bonds have to be broken, which requires work (W). This work will be proportional to the amount of molecules on the created surface area (A) and the surface energy or surface tension (σ). σ is the free energy that must be supplied to increase the surface area of a medium by one unit area. This can be formulated as[18,20]:

$$\sigma = \frac{1}{A}W \qquad\qquad \textbf{2.1}$$
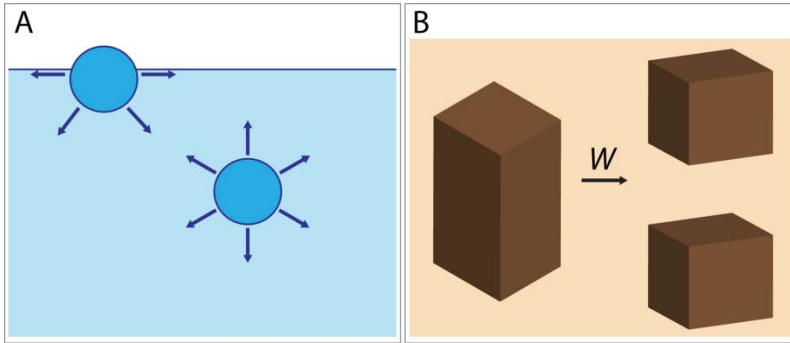
Figure 2.1 Surface free energy. *(A) The molecules in the bulk vs. at the surface of a liquid. The molecule in the bulk of a liquid experiences favorable cohesive interactions with its neighboring molecules; while the molecule at the surface of the liquid experiences disrupted, unsatisfied cohesive interactions. (B) Separation of a block of solid material into two pieces requires the breakage of molecular bonds, requiring work (W). As a result of both (A) and (B) surface atoms possess energy which they tend to reduce. This energy is called surface free energy.*

Note: The unit of surface energy for solid surfaces is energy per unit area (J/m^2). Surface tension (σ) is the tangential stress (force per unit length: N/m) on the surface layer. This stress should be counteracted by the external forces or volume stresses in the body. For example, if a needle is placed on a water surface, it will float because of surface tension. The needle applies a force F_w (its weight) to the surface.

The water will counterbalance it with tangential surface tension forces F_s (**Figure 2.2**).
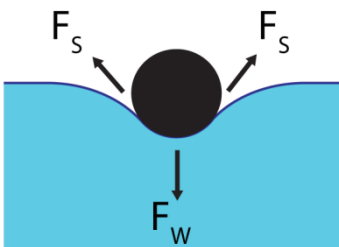
Figure 2.2 Surface tension. *The black circle represents the cross section of a needle floating on water. The weight of the needle depresses the liquid (F_w) and is counterbalanced by surface tension forces (F_s) on both sides.*

The relation between surface tension σ and surface free energy (F) is written as [21]:

$$\sigma = F + A(\frac{dF}{dA}) \qquad\qquad \textbf{2.2}$$

High energy surfaces ($\sigma >$ 500 mN/m[22]) are composed of atoms or molecules which are attached to each other with chemical bonds (covalent, ionic or metallic). A few examples are metals, diamond, (silica) glasses, and ceramics. The molecules of low energy surfaces ($\sigma <$ 50 mN/m[22]) are attached to each other with Van der Waals interactions or hydrogen bonds. It is evident that the intermolecular forces which determine the surface energy of a substance also determine its latent heat and boiling point. Therefore substances such as metals with high boiling points (T > 2000°C) usually have high surface energies[20].

2.2 Interfaces and wetting phenomena

Surfaces tend to minimize their surface free energy, and do so by different means. One of these means is surface relaxation, the rearrangement of surface atoms inwards, mostly observed in liquids since solid atoms are more rigid[19]. A daily life example is wet hair: when dry, hair is likely to be straight and thick and when wet, it sticks together and curves. Other means are to rearrange dangling surface bonds into new chemical bonds[19], further surface energy reduction through physical or chemical adsorption, i.e., forming covalent bonds between surface atoms and reactive chemical species. Hydroxy groups on the surface of silicon, and hydrogen atoms terminating carbon atoms at a diamond surface are examples[19]. Weaker bonds like Van der Waals or hydrogen bonds with a liquid interface are the dominating means to reduce the surface energy of a substrate, known as *surface wetting*[18,23]. Wetting refers to the tendency of a liquid to spread on a solid surface[18,20,24]. Wettability depends on the chemical nature and the roughness of the surface. Density and structure of OH^- groups on solid surfaces, such as silicon or silica, have significant influence on the wettability[24]. Simulations on silica have shown that the degree of wettability is linked to the amount of hydroxyl groups present on the surface[25].

The wettability of a surface can be quantified by a 'contact angle', the angle of a liquid-vapor interface meeting a solid surface. At the edge of the droplet there are three interfaces, the interface between liquid and solid surface (γ_{LS}), the interface between liquid and vapor (γ_{LV}) and the interface between solid and vapor (γ_{SV}) (**Figure 2.3**).
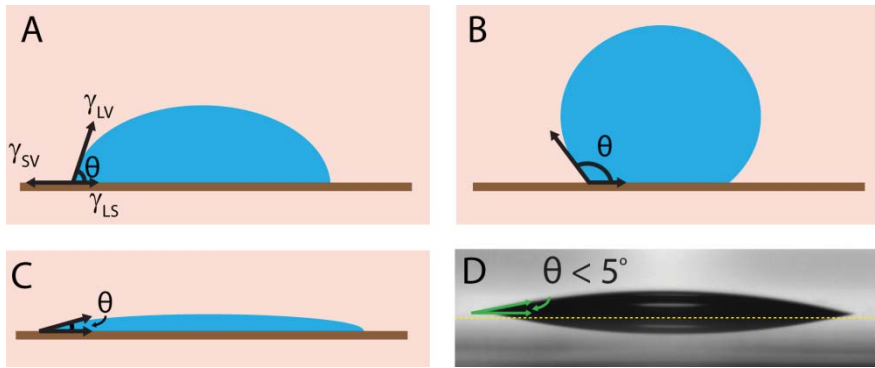
Figure 2.3 Contact angle. *(A) A water droplet wetting a solid surface. Surface tensions at the 3 different interfaces, liquid-vapor (γ_{LV}), liquid-solid (γ_{LS}) and solid-vapor (γ_{SV}) determine the contact angle θ. (B) Water droplet on a hydrophobic surface. θ > 90⁰. (C) Water droplet on a hydrophilic surface. θ < 90⁰. (D) Water droplet on a SiO₂ substrate (Contact angle instrument: Theta, Biolin Scientific, Sweden). The surface line is marked with the yellow dashed line. θ is below 5⁰.*

Young's equation[18] is the simplified energy balance of the three vectors of surface free energies at three different interfaces around the droplet (**Figure 2.3 A**). The force balance can be expressed as below:

$$\gamma_{SV} = \gamma_{LS} + \gamma_{LV} \, cos\theta \qquad\qquad \textbf{2.3}$$

The contact angle of hydrophobic surfaces are above 90⁰ (**Figure 2.3 B**) and for hydrophilic surfaces the contact angle is below 90⁰(**Figure 2.3 C and D**). Interfacial surface free energy is not the only parameter which influences the contact angle. Roughness can have a more significant impact on the observed contact angle, which was originally reported by Wenzel in 1936 [26]. According to Nychka et al.[24], if the value of roughness is below 0.2 mm, the surface can be considered to be completely flat, and the roughness is not expected to affect the observed contact angle. However, extreme surface texture, as investigated by Cassie and Baxter, is an important feature which also influences the contact angle[27]. On such surfaces, extreme roughness is created by using artificial, micro- or nanofabricated pillars. Due to these pillars, the surface texture becomes so high that air is entrapped between the droplet and the substrate, and only a fraction of the solid interface becomes exposed to the droplet. With this extreme texture, a hydrophilic surface can

be transformed into a *super-hydrophobic surface*[24,28]. By this mechanism, many biological species (including self-cleaning lotus leaves) are capable of controlling wetting. Various commercial products such as self-cleaning paints and non-sticky containers, which benefit from these extreme textures, are available today[24,29].

The spreading of a fluid lipid film on a surface can be perceived in terms of a wetting phenomenon, which occurs upon formation of the surface-membrane interface, and is driven by the resulting gain in free energy [30-32]. If a source is available, which is capable of providing a continuous supply of lipid molecules, membranes can draw material from the source and spread laterally, expanding the membrane-solid interface. The available surface area becomes increasingly covered by the membrane. Most of the experimental work described later in this thesis involves wetting of a silicon dioxide surface with a continuously spreading double bilayer lipid film. The details of the formation of this membrane will be discussed in the next chapter.

Chapter 3 : BIOPHYSICS OF LIPID MEMBRANES

3.1 The lipid molecule

Lipids are amphiphilic molecules, which contain both a hydrophilic (polar) and a hydrophobic (non-polar) moiety in their molecular structure. They are categorized as polyketides, acylglycerols, sphingolipids, prenols, or saccharolipids[33], based on the chemical nature of their backbone. Among the glycerolipids are phospholipids, which are the main constituent of biological cell membranes. When fully hydrolyzed, phospholipids break down into smaller units: fatty acids, glycerol, a phosphate, and a small organic molecule constituting the headgroup, such as choline[33]. The hydrophobic part of a phospholipid molecule consists of fatty acid chains, which are organic hydrocarbons without any charged moieties. The simple polyol glycerol, together with the negatively charged phosphate group and the charged or neutral headgroup, constitute the hydrophilic part of the molecule.

Currently it is known that the variation of head groups and aliphatic chains allows (potentially) 100,000 lipid species to exist in eukaryotic cells[34-35]. In recent analytical studies nearly 600 individual lipid species were detected and quantified[36] in human blood serum. Such a large variety should serve a great number of functions[37]. Although lipids abundantly exist in biological organisms, for many years they were believed to be the most inert molecules, acting only as an energy source and as a barrier for cells or organelles. Today, we are still far from having a complete picture, but some more crucial functions of lipids have been acknowledged: membrane trafficking, regulation of membrane proteins, facilitating signal transduction and molecular recognition [4]. Such involvement of lipids in metabolic functions have lead to the emergence of the research field of lipidomics, which studies how the diversity of lipids correlates to certain metabolic roles in biological organisms[34-35,38]. To give one example, the malfunctioning of sphingolipid catabolism was recently linked to Alzheimer's disease[39].

Considering the large structural diversity of lipids, one can predict that there are also many possibilities of lipid interaction with proteins or other lipids. Probably the most important of them is the ability to 'self-assemble' into mesoscale membrane structures.

3.2 Self-assembly of lipids

When placed in an aqueous solution, lipid molecules spontaneously self-assemble to form lipid bilayers. By means of self assembly, the individual lipid molecules adopt an ordered arrangement, which has different physical properties than the individual molecule. Self-assembly of lipids is a thermodynamically driven process. When water molecules come in contact with a non-polar molecule, H-bonds between water molecules are lost [20]. If the molecule is small, water molecules salvage the lost H-bonds by packing around it without terminating any bonding, forming clathrate cages. This restructuring mechanism is known as hydrophobic solvation/hydration. The high desire of water for keeping H-bonds will thus be satisfied, however, the order of water molecules will increase enormously. Hydrophobic hydration is the main driving force for the self-assembly of lipids.

If one single lipid-like molecule (a hydrocarbon chain) is placed in water, a water cage will form around the hydrophobic entity of the molecule (**Figure 3.1**). This is a very rigid configuration with a high degree of order and naturally leads to decreased entropy. During self-assembly, the change in the Gibbs free energy (ΔG) of the system is

$$\Delta G = \Delta H - T\Delta S \qquad \textbf{3.1}$$

where ΔH is the change in enthalpy and $T\Delta S$ the change in entropy. The system will always tend to increase its entropy and minimize its free energy. Self-assembly is a favored process, as it removes lipid molecules from exposure to water and restores hydrogen bonding, which increases the system entropy and accordingly reduces the free energy. As a result of this, lipid molecules spontaneously self-assemble into more organized structures. The morphology of such assemblies varies greatly, depending on external conditions such as temperature and lipid concentration. This will be discussed in greater detail in section **3.5 Lipid polymorphism.**

One of the most important self-assembled lipid structures is the bilayer. A lipid bilayer consists of 2 leaflets of self-assembled lipid molecules, where the

Figure 3.1 Water caging around a single lipid-like molecule. *(A) Side view and (B) top view of the first coordintation shell of water around a lipid-like molecule (blue), which was optimized using a semi-empirical geometry optimization (PM3), by means of the Gaussian 09 software package (Gaussian Inc., CT, USA). The hydrogen bonding of one water molecule with the three other neighbouring water molecules is depicted with yellow dashed lines in (A). The water molecules posess a tetrahydral arrangement with 4 H-bonds. The 4th H-bond (not shown) is pointing out of the page plane, interacting with one of the water molecules in the second layer.*
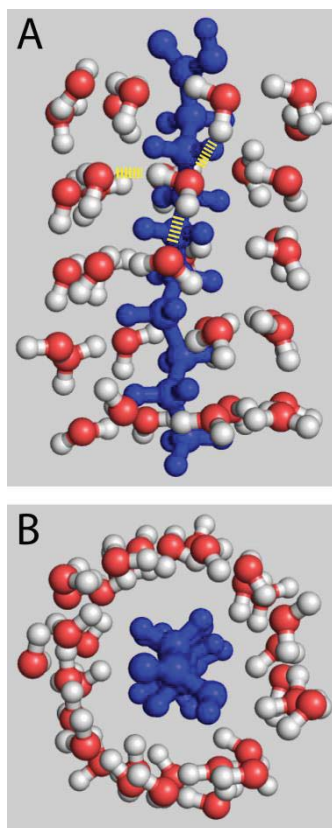
hydrophobic tails face each other, and the hydrophilic parts of the molecules face outwards. Water is essentially excluded from the hydrophobic regions and is in contact only with the hydrophilic moieties. The sheets of the bilayer are held together by hydrophobic interactions, the strong attraction forces of hydrophobic molecules in water. For molecules such as methane, cyclohexane or benzene, the magnitude of the hydrophobic interactions is approximately 350 times stronger than the Van der Waals interaction potentials[20].

Another term in the Gibbs free energy equation **3.1** is the enthalpy ΔH. In the liquid state, each water molecule participates in 3-3.5 H-bonds. However, around a non-polar solute molecule, water can have a higher coordination of 4 H-bonds (yellow dashed lines in **Figure 3.1 A**) which leads to a lower ΔH. This contribution is rather small, it constitutes only 15% or less of the total free energy change[20].

3.3 Membrane mechanics

Lipid membranes are only a few nanometers thick, while in the other 2-dimensions they can extend to hundreds of micrometers. The lipid membrane can be treated as an infinitely thin elastic sheet, for which the elastic energy F is described as

$$F = \int dA \left[\frac{\kappa}{2}(c_1 + c_2 - c_0)^2 + \bar{\kappa}c_1 c_2 + \sigma \right] \qquad \textbf{3.2}$$

The first term inside the integral refers to the bending of a lipid membrane. dA is the surface area element, κ is the bending rigidity, c_1 and c_2 are the two principle curvatures of the membrane. c_0 is the spontaneous curvature accounting for a possible asymmetry between the two monolayer leaflets. This term becomes important if, for instance, the membrane is composed of different lipids in the inner and in the outer monolayer leaflet.

The second term is the Gaussian curvature term $\bar{\kappa}c_1 c_2$, where $\bar{\kappa}$ is the Gaussian modulus. This term becomes only important if the membrane topology changes, i.e., a spherical vesicle forms a donut shaped vesicle. For a flat lipid membrane which only undergoes simple shape changes, this term is omitted. The importance of bilayer membrane bending for the studies in this thesis will be explained in next sub-chapter **3.4 Formation of vesicles from membranes**.

The first and second term inside the integral were described in 1973 by Helfrich[40] as *membrane curvature energy*.

The third term σ is the membrane tension. Membrane tension can be dissected into two terms for low (entropic) and high tension (stretching) regimes. **Figure 3.2** depicts shape forms of lipid membranes under these tension regimes.

The lipid membrane under low tension is caused by thermal undulations (**Figure 3.2 A**) and the relation between tension and area expansion is:

$$\sigma \sim \kappa q_{min}{}^2 \exp\left[\frac{8\pi\kappa}{k_B T} \frac{\Delta A}{A_0} \right] \qquad \textbf{3.3}$$
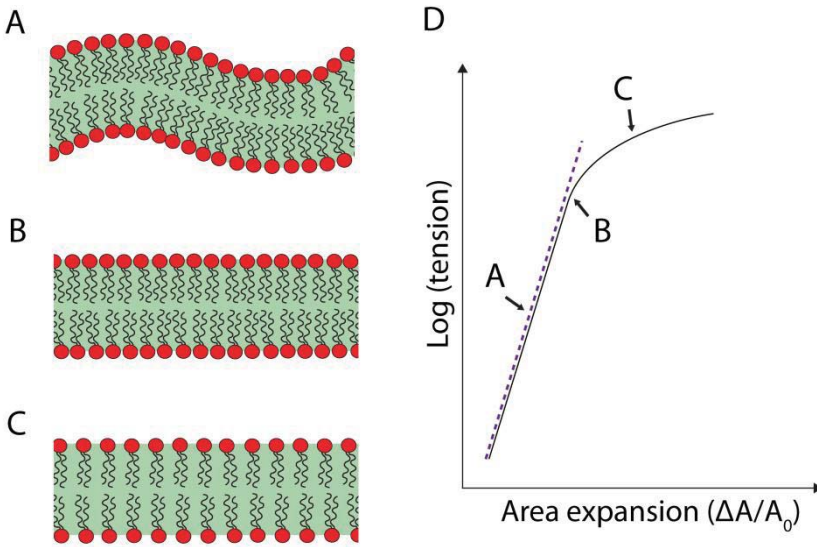
Figure 3.2 Tension of phospholipid membranes as a function of stretching.
*(A) Schematic of the cross sectional profile of a phospholipid membrane under low
tension. The membrane bends as a result of thermal fluctuations. (B) Schematic of the
cross sectional profile of a phospholipid membrane under high tension. The membrane
is free of undulations. (C) A stretched phospholipid membrane. The distance between
individual lipid molecules is increased. (D) Representative log-plot of membrane tension
vs. membrane stretching. The membrane experiences different tension regimes which
are depicted on the left panels. Each phase is marked with the corresponding letters. A
dashed line helps to identify the transition from regime A to B.*

where A_0 is the initial area of the membrane and $A - A_0$ is the expansion of
the membrane due to mechanical stretching. q_{min} is the cut-off wave vector
of the membrane fluctuations:

$$q_{min} = \frac{2\pi}{\lambda_{max}}$$
      3.4

where λ_{max} is the largest wavelength of the membrane. If the membrane is
continuously mechanically pulled in lateral direction, it will become flat and
free of fluctuations (**Figure 3.2 B**). Once flattened, continuous mechanical
stress will initiate the stretching of the membrane, i.e., the distance of the
individual lipid molecules from each other will increase (**Figure 3.2 C**).
Under these conditions, the membrane tension is linearly proportional to the
area expansion:

$$\sigma \sim K_s(\frac{\Delta A}{A_0}) \qquad\qquad 3.5$$

where K_s is the stretching modulus.

Rawicz, Evans et al. [41] have experimentally investigated tension in the membrane as a function of stretching. By aspirating a lipid vesicle with Evan's micropipette, the lipid membrane is stretched. The aspiration pressure acts as the source of lateral tension, and area expansion as a response is measured from recorded micrographs. A representative graph adapted from their findings showing the relation of membrane tension and membrane stretching is depicted in **Figure 3.2 D**.

The plot reveals initially non-linear entropic and subsequently linear elasticity of the lipid membrane. Entropic elasticity is typical behavior for any type of soft matter, e.g. rubber [42]. According to the findings of Rawicz et al.[41], the lipid membrane can be stretched up to 5% ($\Delta A/A_0 = 0.05$). In other words, lipid membranes are reluctant to stretching.

3.4 Formation of vesicles from membranes

Until now, I have covered the formation of flat lipid bilayers due to hydrophobic interactions. However, the plasma membranes of living cells or lipid vesicles are spherical membrane structures with a defined internal volume. The answer to the question why membranes form closed compartments is related to the interplay between bending energy (E_{bend}) (mentioned above in sub-chapter **3.3 Membrane mechanics**) and the edge tension energy (E_{edge}) of the bilayer[43].

Assume that we have a flat circular patch of a bilayer. Lipid molecules at the circumference of this disc-shaped membrane (**Figure 3.3 A**) will arrange themselves in a way that the hydrophobic parts of the molecule will avoid water, and form a micelle-like (*cf.* **3.5 Lipid polymorphism**) membrane edge (inset in **Figure 3.3 A**), which is characterized by an edge tension. The edge energy of the membrane is:

$$E_{edge} = 2\pi r \gamma \qquad\qquad 3.6$$

where r is the radius of the open circular membrane patch, and γ is the edge tension (5-10 pN[44-45]). The bending energy of the membrane is

$$E_{bend} = 4\pi \left(2\kappa + \bar{\kappa}\right) \qquad \textbf{3.7}$$

where κ and $\bar{\kappa}$ are the bending and Gaussian moduli of the membrane, respectively. A typical value for κ is $10 - 20\ k_b T^{41,46}$. $(k_b T_{room} = 4\ x\ 10^{-21} J)$. The Gaussian modulus $\bar{\kappa}$ is in the same order of magnitude as κ and negative[47-48].
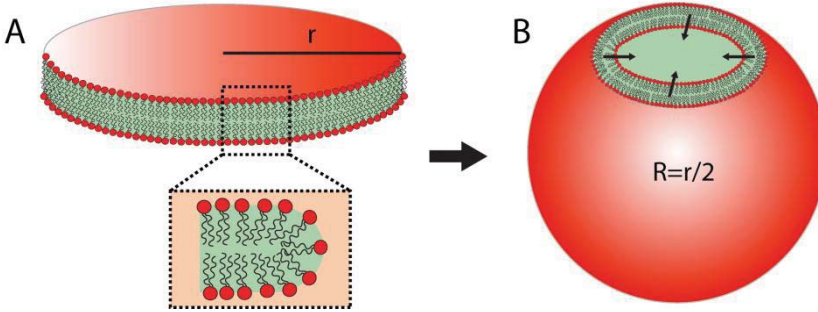
Figure 3.3 Formation of vesicles from a flat membrane. *(A) A schematic drawing of a circular flat bilayer lipid membrane with radius r. In reality the edges of such a planar bilayer would be curved to a structure reminiscent of micelles (inset). (B) The closure of a flat membrane to a spherical vesicle. The energy gained by reducing the edge length is greater than the energy cost of bending.*

Vesicle formation will occur (**Figure 3.3 B**) if the edge tension energy is greater than the bending energy cost of curving a flat membrane to a vesicle. The ratio E_{bend}/E_{edge} will determine the critical vesicle radius. If this ratio is smaller than 1, a vesicle will form.

$$\frac{E_{bend}}{E_{edge}} < 1 \Rightarrow \frac{4\pi\left(2\kappa + \bar{\kappa}\right)}{2\pi r \gamma} < 1 \Rightarrow r > \frac{2\left(2\kappa + \bar{\kappa}\right)}{\gamma} \qquad \textbf{3.8}$$

This implies that r must be larger than $\frac{20 k_b T}{10 \text{pN}}$ ($\sim$ nm). The minimum vesicle size (minimum aggregate radius) is therefore estimated to be on the order of a few nanometers. This means that any lipid bilayers with dimensions larger than a few nanometers is shape-instable and will form a closed membrane, i.e., a vesicle[49]. This effectively means that all freestanding (unsupported) bilayer membranes exist in the form of vesicles.
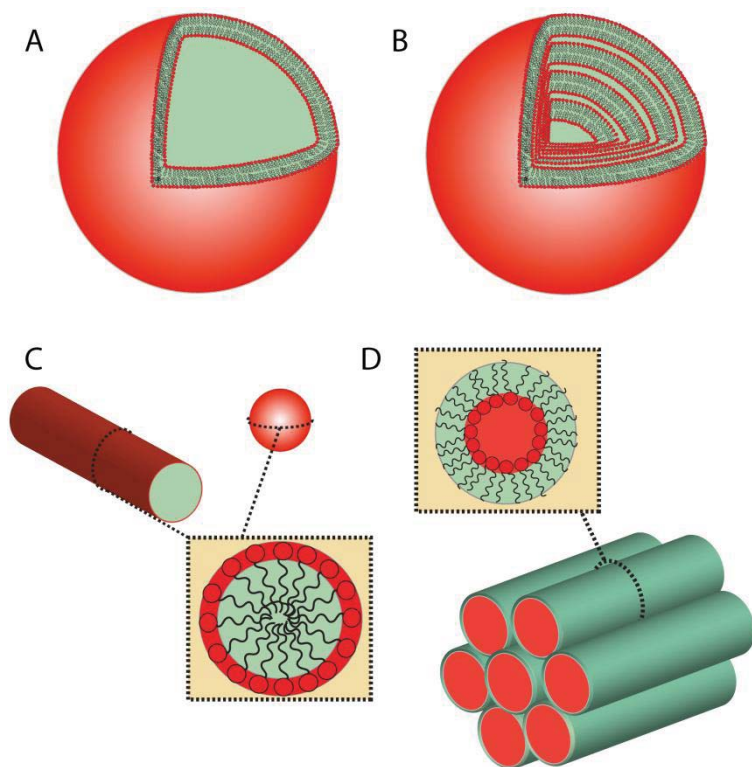
3.5 Lipid polymorphism

In the previous section, I have discussed the energetic situation associated with the transformation of a flat membrane into a spherical vesicle. These vesicles consist of a single bilayer membrane encapsulating an interior volume of the solvent they are suspended in, which is typically an aqueous buffer. Due to the single membrane boundary, the vesicles are referred to as unilamellar vesicles or liposomes (**Figure 3.4 A**). Biological cells consist of an interior volume of greater complexity than a vesicle, but they are also surrounded by a unilamellar (plasma) membrane decorated with membrane proteins and other structural elements. Due to this structural similarity, liposomes are useful as biomimetic model systems to study certain membrane-related cell properties and behavior. Another form of spherical lipid assembly is the multilamellar vesicle (**Figure 3.4 B**), in which multiple sheets of bilayer membranes are stacked, similar to the cell layers in an onion (onion shell vesicle). In later sections of this chapter I will describe the conditions under which a unilamellar vesicle can be dynamically extracted from a multilamellar vesicle. The multilamellar vesicle is used as a lipid reservoir, compensating for the tension changes of the unilamellar vesicle and supplying lipids accordingly. Similar lipid-rich reservoirs do exist in biological cells. Lipid droplets[16] or wrinkled fragments of plasma membranes[17] act as lipid sources balancing the membrane tension.

Vesicles are, however, not the only type of self- assembled structure composed of surfactant molecules. There are various geometries that surfactant assemblies can assume, depending on different factors, but most dominantly, the structure of the individual surfactant. This shape-related dependency can be defined by a surfactant packing parameter[22,43]: $V/(Al)$, where V is the volume of the hydrophobic domain of the surfactant molecule, A is the interfacial area between hydrophobic and hydrophilic domain, and l is the length normal to the interface, i.e., the length of the hydrophobic chain. Many commonly used phospholipids have a packing parameter around 1. This entails that they assemble in bilayer membranes (**Figure 3.4 A and B**). Surfactants with bulky head groups (packing parameter< 0.5) prefer to form micellar structures (**Figure 3.4 C**), whereas those with large hydrophobic tails (packing parameter > 1) form reversed crystal phases (**Figure 3.4 D**).

Besides the ratio of the hydrophobic to hydrophilic moiety, there are other factors which affect the packing parameter. Ionic strength, pH, temperature or saturation level of the hydrocarbon chains are among these factors[48,50]. In the presence of a solvent, a lipid assembly will adopt certain structural

arrangements, referred to as lipid phases. Such phases can be categorized based on the morphology of the individual layers, as lamellar and non-lamellar phases. Lamellar phases involve a bilayer membrane as shown in (**Figure 3.4 A and B**). Non-lamellar phases can contain micelles (**Figure 3.4 C**), hexagonal phases (H_{II}) (**Figure 3.4 D**) or more complex arrangements like porous cubic phases[51]. Seddon and Templer[48] have listed 23 different phases of lipids, of which only the fluid lamellar phases (L_α), are used in the content of this thesis.

Figure 3.4 Lipid polymorphism. *(A) Unilamellar vesicle. A spherical volume of water is surrounded by a single intact bilayer. (B) Multilamellar vesicle. Lipid bilayer membranes are arranged in an onion-shell like fashion. (C) Spherical and tubular micelles. (D) Inverted hexagonal structures (H_{II} phase)[48]. Each hexagon consist of 7 cylinders. Note that in this arrangement, the hydrocarbon chains of the lipid molecules face outwards, and lipid headgroups inwards. The magnifications in C and D show the cross sections of each individual structure.*
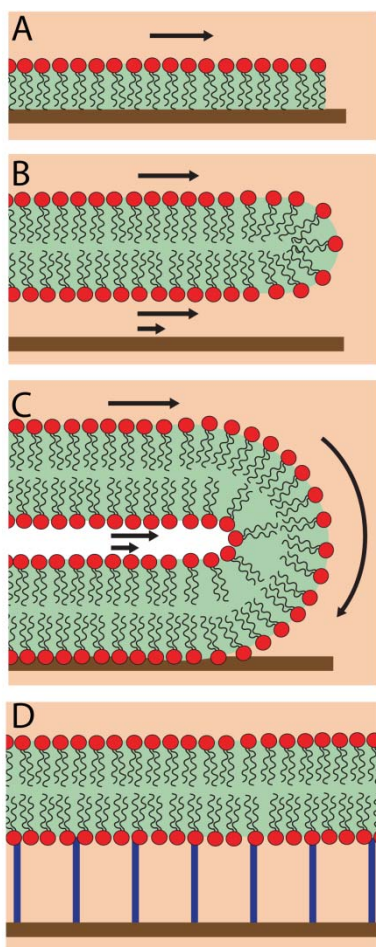
3.6 Supported membranes

So far, I considered only the behavior of free-standing lipid membranes in bulk solutions. In this section I will discuss the self assembly of lipid membranes on solid surfaces. When lipid aggregates interact with a flat solid interface, they self-organize and form supported membranes[6,22,32]. The details of this formation will be provided in **3.7 Formation of supported membranes**. Solid-supported membranes are of large practical interest as model systems to study the features of the plasma membranes of biological cells. They have advantages over other types of model membranes such as vesicles or Langmuir-Blodgett films: The solid surface support provides greater stability, membrane fabrication is more versatile and controlled, and a broader range of instrumentation for imaging and analysis is available[52].

Depending on the surface properties of solid supports, the membranes self-assemble in different ways. On hydrophobic, low energy substrates such as photoresists or fluorinated polymers, e.g. SU-8, EPON, Teflon AF, the lipids self assemble as monomolecular layers, where the hydrophobic chains of a single layered lipid film face the substrate (**Figure 3.5 A**)[22]. Although monolayers do not represent plasma membranes very well, as they consist of only half a bilayer and cannot incorporate proteins, they have unique advantages: indifference to the ambient buffer composition, long shelf life of hydrophobic supports, further structural simplicity and versatility.

The most commonly studied type of supported membranes, which are well suitable as mimics for the cell's plasma membrane, are supported bilayers (**Figure 3.5 B**)[6,22,31-32]. Lipid bilayers can be formed on many hydrophilic high energy surfaces: metals, metal oxides, semi conductor oxides and nitrites, quartz, mica and borosilicate glass. These surfaces are mostly optically transparent and are therefore compatible with optical microscopy techniques. A closely related variant of the supported bilayers are the tethered, or cushioned, bilayers[53-54] (**Figure 3.5 D**). These lipid films feature spacer molecules (tethers), which establish a larger gap between the solid surface and the bilayer than observed in conventional supported bilayers. The spacer molecules are usually polymer chains (e.g. polyethylene glycol (PEG), branched polyethylene imine (PEI), dextran), which provide an elastic cushion for the membrane. The main purpose is to allow for incorporation of membrane proteins, for example ion channels or receptors, which protrude from both sides of the membrane. Tethered bilayers offer interesting possibilities, but also disadvantages. The lateral mobility of both the lipids in

the bilayer, and of the integrated proteins, is reduced due to the grafting of the lipid-anchored polymer to the substrate.


Figure 3.5 Solid supported membranes. *(A) Solid-supported monolayer. The hydrophobic tails of the lipid molecules face the solid support. (B) Solid-supported bilayers. A spreading bilayer is sliding on the solid support. (C) Solid supported double bilayer. The membrane is rolling on the support by a tank-thread motion. The lower (proximal) bilayer is fixed on the substrate while the upper (distal) bilayer slides over the proximal bilayer and rolls onto the solid substrate. (D) Tethered bilayer membrane. Note the large spacing between the bilayer and the solid support.*

An alternative approach to membrane assembly on high energy surfaces is the double bilayer spreading[6,32] (**Figure 3.5 C**). In this variant of phospholipid film formation on a solid support, two connected lipid bilayers are stacked, with a thin water layer in between them. The experimental work on double-bilayer phospholipid membranes is the main theme of this thesis, which conceptually connects the individual studies.

3.7 Formation of supported membranes

There are various means to form or pattern supported membranes. Two classic methods are the Langmuir-Blodgett[22,55] and the Langmuir-Schaefer[22,56] (a variant of the first) deposition, where the lipid molecules at an air-water interface are forced to migrate onto a submerged substrate. Another abundantly used method involves vesicle rupture. A vesicle suspension is deposited onto a surface, followed by adhesion and rupture of the vesicles, forming small bilayer patches. The edges of the flat bilayer patches merge into a continuous bilayer film[57]. There are also means to fabricate micro- and nano-patterned supported membranes with high spatial precision. A recent review by Czolkos *et al.*[22] is discussing various aspects of these methods in detail.

In my experimental work I have fabricated double bilayer membranes by means of circular self-spreading of a multilamellar reservoir. I exploited that a double bilayer spontaneously emerges from a surface adhered multilamellar (onion shell) liposome by a surface wetting mechanism (**2.2 Interfaces and wetting phenomena**). Very little detail is currently known about the internal organization of a MLV, but it is clearly difficult to picture double bilayer spreading from a perfect, i.e., defect-free, MLV (**Figure 3.6 A**).
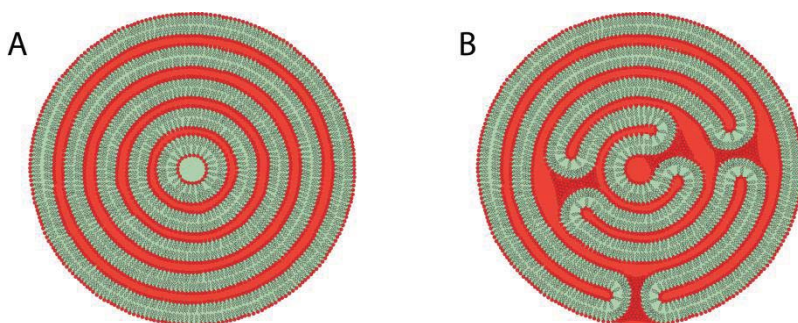
Figure 3.6 Internal organization of bilayers in a multilamellar vesicle (MLV). *(A) A schematic representation of a defect-free multilamellar vesicle. The individual bilayers are not interconnected. (B) Cross section of an alternative structure of a multilamellar vesicle, which shows that the onion-shell layers are connected to each other via handle-like defects. Note that the drawing is simplified and an actual MLV consists of hundreds of bilayers.*

Such a mechanism would require rupturing of the layers of the MLV, and re-assembly into a pair of bilayers. The evidence in the previous studies by Leng

et al.[58] or Paper V in this thesis, points to a different situation. These findings suggest that the layers are rather connected to each other by nanochannels (**Figure 3.6 B**), which can be perceived as handle-like pores, semi-pores or micelle like defects. The MLV does not have to rupture in order to supply membrane in this way, and can spread on a substrate as a continuous double-bilayer membrane.

The spreading of lipids from a MLV can be described assuming tension driven flow, which is often referred to as Marangoni flow[18,59-60]: it is the convective flow of lipids driven by a surface tension gradient. The driving force for such a flow would be a free energy gain in the system. This energy gain emanates from the difference in surface tension at two different interfaces: the substrate wetted with the aqueous buffer (σ_A) and the substrate wetted with the lipid film (σ_L) (**Figure 3.7**). For lipid spreading to be favorable the latter should be lower. The overall tension (σ_s) then is:

$$\sigma_s = \sigma_A - \sigma_L \qquad \textbf{3.9}$$

The MLV from which the lipids are drawn also has an internal tension (σ_0), which opposes the spreading. The spreading power (S) can thus be formulated as the difference between the energy gain by wetting and the tension of the reservoir:

$$S = \sigma_s - \sigma_0 = \sigma_A - \sigma_L - \sigma_0 \qquad \textbf{3.10}$$

For S > 0 the wetting is favorable. In this case $\sigma_s > \sigma_0$ and $\sigma_L < \sigma_A$.

An important factor contributing to the surface adhesion of the lipid film is the presence of fusogenic agents. On hydrophilic, negatively charged surfaces the adhesion of the membrane to the surface is known to be

facilitated by buffers with high ionic strength[59,61-62], in particular when multivalent ions, e.g. Ca^{2+}, Mg^{2+}, Eu^{3+}, are present, which screen the negative charges of the lipids and the surface. This also indicates that the lipids are not directly in contact with the solid substrate, but separated by a thin layer of water. Divalent cations, especially Ca^{2+} in low millimolar concentrations, are known to have a dramatic effect on the surface potential. Compared with monovalent salts, divalent cations are already equally effective at about a 100 times lower concentrations[20].
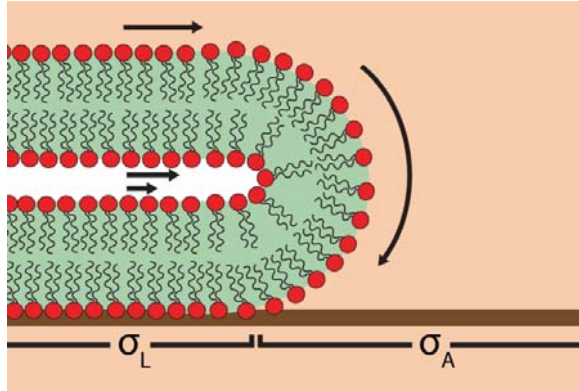
Figure 3.7 The surface tension during double bilayer lipid spreading. *The substrate wetted by the lipid has a lower surface tension (σ_L) than the substrate wetted by the aquous solution (σ_A). The system gains energy by wetting the surface with a lipid film, i.e., the free energy of the system is reduced.*

In most experiments described in this thesis, I used multivalent cations, Ca^{2+} or Eu^{3+} to enhance wetting. Furthermore, even if the bulk concentration of Ca^{2+} is relatively lower than the concentration of monovalent salts in a solution, the local concentration of Ca^{2+} on the surface can be much higher[20]. On negatively charged surfaces such as SiO_2, divalent ions often bind chemically to available functional groups (e.g. Si-O⁻) and reduce the surface charge density. Ca^{2+} concentrations of a few mM, or 10^{-5} M of trivalent ions such as La^{3+}, are enough to efficiently neutralize a negatively charged surface and can even result in charge reversal, i.e., a build-up of positive surface charges as cations continue to adsorb onto the surface[20].

The experimental foundations for single and double bilayer spreading and the theoretical foundations for single bilayer spreading from a lipid source were previously established by Sackmann[6], Rädler[31] and Nissen[32]. Nissen et al.[32] identified different spreading modes for single bilayer membranes with varying cholesterol, cationic lipid content or temperature. These modes could be distinguished by a kinetic spreading coefficient (β) (m^2/s), which is related to the membrane velocity $v(t)$

$$v(t) = \sqrt{\frac{\beta}{t}}$$

3.11

The spreading power S, which quantifies the driving force for the spreading process, is related to the spreading and the friction coefficients:

$$\beta = \frac{S}{2\zeta} \qquad\qquad \textbf{3.12}$$

In order to obtain the spreading coefficient for a double bilayer membrane, I adapt a one-dimensional model which was developed by Rädler for single bilayers. **Figure 3.8** is a schematic drawing of the propagation of a single and a double bilayer. According to a study by Rädler, Strey and Sackmann, a single bilayer propagates (in most cases) by a sliding motion, while the double bilayer propagates by a tank thread motion. This localizes the effective friction between bilayer and surface for the first case, and between the two stacked bilayers in the second case.
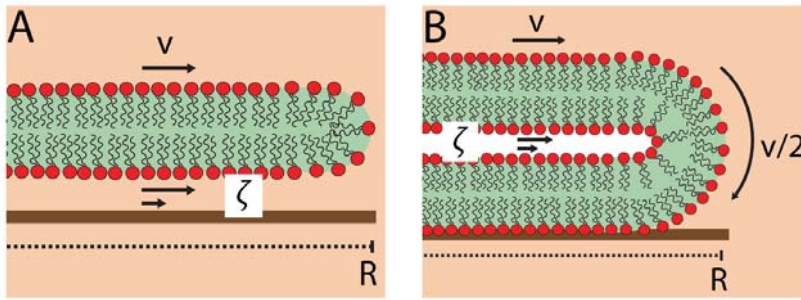
Figure 3.8 Spreading coefficient for a 1D model. *(A) A sliding single bilayer. The membrane velocity is depicted as v. (B) A spreading double bilayer membrane. The membrane velocity at the rolling edge is half the velocity of the membrane. The length of the spread is R (between the reservoir and the spreading front). Note that the spreading coefficients are effective in different regions for each spreading mode: friction is effective between the bilayer and the surface in (A) and between the two bilayers in (B).*

Some assumptions are valid for both the single and the double bilayer membrane model:

i) The tension gradient ($\nabla\sigma$) drives the spreading process and it is balanced by the frictional stress.

$$\zeta\vec{v} = \nabla\sigma \Rightarrow \zeta v = \frac{d\sigma}{dx} \qquad\qquad \textbf{3.13}$$

where v is the membrane velocity. For a single bilayer, ζ represents the friction coefficient between the surface and the bilayer. For a double bilayer membrane, ζ is the friction coefficient between the proximal and distal bilayer.

ii) In a first degree of approximation, the membrane is incompressible[30-31]:

$$\nabla \vec{v} = 0 \;\Rightarrow \frac{dv}{dx} = 0 \qquad\qquad \textbf{3.14}$$

Combining equations **3.13** and **3.14** leads to:

$$\frac{d^2\sigma}{dx^2} = 0 \Rightarrow \; \sigma = ax + b \qquad\qquad \textbf{3.15}$$

$\sigma(R)=\sigma_S$, where σ_S is the tension due to the adhesion to the surface. $\sigma(0)=\sigma_0$, where σ_0 is the tension of the multilamellar reservoir.

$$\sigma = \frac{\sigma_S - \sigma_0}{R}x + \sigma_0 \qquad\qquad \textbf{3.16}$$

Combining equation **3.13** with **3.16** leads to:

$$\zeta v = \frac{\sigma_S - \sigma_0}{R} \qquad\qquad \textbf{3.17}$$

Re-arranging equation **3.17** gives $\zeta vR = \sigma_S - \sigma_0$, showing that the membrane flow caused by the tension difference over radius R is opposed by the friction. From this point on, bilayer and double bilayer spreading have to be considered separately. The velocity at the spreading edge of the double bilayer v_R will be half the velocity of the membrane v, since the spreading edge of the double bilayer exhibits rolling motion, where only half of the membrane material is laid upon the substrate.

Single bilayer membrane (1D)   Double bilayer membrane (1D)
              (**Figure 3.8 A**)   (**Figure 3.8 B**)

$$v = \frac{dR}{dt} \qquad \textbf{3.18a}$$

$$v = 2\frac{dR}{dt} \qquad \textbf{3.18b}$$

Inserting equation **3.18a** and **3.18b** into equation **3.17** leads to

$$\zeta \frac{dR}{dt} R = \sigma_S - \sigma_0 \qquad \textbf{3.19a}$$

$$\zeta 2\frac{dR}{dt} R = \sigma_S - \sigma_0 \qquad \textbf{3.19b}$$

Integrating the left side of equations **3.19a** and **3.19b**, from R(0) to R(t) and the right side of the equations from t=0 to t gives

$$\zeta \frac{1}{2} R^2(t) = (\sigma_S - \sigma_0)t \qquad \textbf{3.20a}$$

$$\zeta R^2(t) = (\sigma_S - \sigma_0)t \qquad \textbf{3.20b}$$

The radius of the spread at t=0: $R(0) = 0$. Rearranging equations **3.20a** and **3.20b** gives:

$$R(t) = \sqrt{\frac{2(\sigma_S - \sigma_0)t}{\zeta}} \qquad \textbf{3.21a}$$

$$R(t) = \sqrt{\frac{(\sigma_S - \sigma_0)t}{\zeta}} \qquad \textbf{3.21b}$$

The derivative of R(t) in equations **3.21a** and **3.21b** with respect to t is the velocity of the membrane v:

$$v = \frac{dR}{dt} = \sqrt{\frac{(\sigma_S - \sigma_0)}{2\zeta t}} \qquad \textbf{3.22a}$$

$$v = \frac{dR}{dt} = \sqrt{\frac{(\sigma_S - \sigma_0)}{4\zeta t}} \qquad \textbf{3.22b}$$

The spreading power $S = \sigma_S - \sigma_0$ is the product of the spreading coefficient and the friction coefficient:

$$\beta = \frac{S}{2\zeta} \qquad \textbf{3.23}$$

Inserting equation **3.23** into equations **3.22a** and **3.22b** will give the spreading coefficient β for single and double bilayer spreading, respectively:

$$v = \sqrt{\frac{\beta}{t}} \qquad \textbf{3.24a} \qquad\qquad \frac{v}{2} = v_R = \sqrt{\frac{\beta}{t}} \qquad \textbf{3.24b}$$

Note that for a single bilayer membrane, the velocity of the spreading edge is the same as the membrane velocity. For a double bilayer membrane, the velocity of the spreading edge at radius R (v_R) is half the membrane velocity (*cf.* **Figure 3.8**).

Now I proceed to a 2D model to describe double-bilayer membrane spreading of a circular patch (**Figure 3.9**).
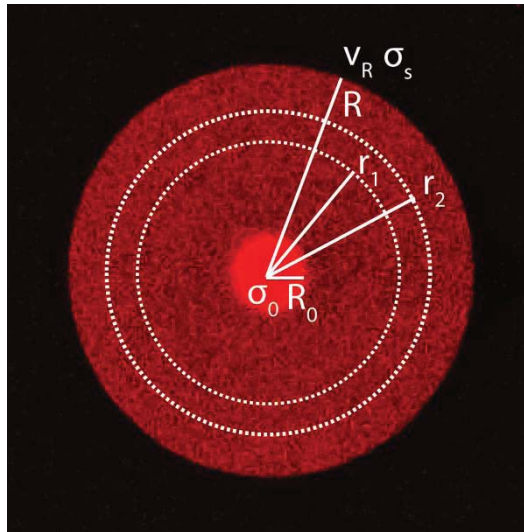
Figure 3.9 2D spreading coefficient. *A laser scanning confocal fluorescence micrograph of a circular lipid spread (top view). The multilamellar reservoir is the bright spot (high emission intensity) in the center of the circle. Two arbitrary circles are drawn with the multilamellar reservoir as their center, having radiuses r_1 and r_2. R is the radius of the entire spread. v_R is the velocity at the spreading edge, and σ_S is the tension caused by adhesion to the surface. r_0 is the radius of the multilamellar reservoir and σ_0 is the reservoir tension.*

Imagine an arbitrary ring on the circular lipid spread with an inner radius r_1 and an outer radius r_2 (**Figure 3.9**). During spreading, the number of lipid molecules in this ring should be constant. This requires, according to the law of mass conservation, that the flux (J) of lipid molecules at r_1 or r_2 must be equal.

$$J_1 = J_2 \qquad \textbf{3.25}$$

The lipid molecules coming from the multilamellar reservoir will pass through r$_1$ with velocity v_1, and subsequently r$_2$ with velocity v_2:

$$2\pi r_1 \rho v_{r_1} = 2\pi r_2 \rho v_{r_2}$$
$$r v_r = constant \qquad \textbf{3.26}$$

The velocity v_r of the lipid molecules at any arbitrary circle of radius r can be related to the velocity v_R of lipids at the spreading edge.

$$r v_r = R v_R \qquad \textbf{3.27}$$

Rearranging equation **3.27** gives $v_r = \frac{R}{r} v_R$. Due to the differences in the velocity parameter, from now on the model will again differ for single and double bilayer membranes.

2D spreading coefficient of a circular single bilayer membrane patch	2D spreading coefficient of a circular double bilayer membrane

$$v_r = \frac{R}{r}\frac{dR}{dt} \qquad \textbf{3.28a} \qquad\qquad v_r = 2\frac{R}{r}\frac{dR}{dt} \qquad \textbf{3.28b}$$

The radial tension gradient drives the spreading process. It is balanced by the frictional stress (**3.13**):

$$\zeta \vec{v} = \nabla \sigma \Rightarrow \zeta v_r = \frac{d\sigma}{dr}$$

Where ζ is the friction coefficient between the surface and the bilayer (left

column), or between the proximal and distal bilayers (right column), respectively.

Inserting equation **3.28a** and **3.28b** into equation 3.13 gives:

$$\zeta v_r = \zeta \frac{R}{r} \frac{dR}{dt} = \frac{d\sigma}{dr} \qquad \textbf{3.29a} \qquad \zeta v_r = \zeta 2 \frac{R}{r} \frac{dR}{dt} = \frac{d\sigma}{dr} \qquad \textbf{3.29b}$$

Integrating equations **3.29a** and **3.29b** from R_0 to R gives

$$\zeta R \frac{dR}{dt} \ln\left(\frac{R}{R_0}\right) = \sigma_s - \sigma_0 \qquad \textbf{3.30a} \qquad 2\zeta R \frac{dR}{dt} \ln\left(\frac{R}{R_0}\right) = \sigma_s - \sigma_0 \qquad \textbf{3.30b}$$

The spreading power ($S = \sigma_S - \sigma_0$) is the product of spreading coefficient and friction coefficient. Equations **3.30a** and **3.30b** are therefore rearranged to obtain the spreading coefficient:

$$R \frac{dR}{dt} \ln\left(\frac{R}{R_0}\right) = \frac{\sigma_s - \sigma_0}{\zeta} = 2\beta \qquad \textbf{3.31a} \qquad R \frac{dR}{dt} \ln\left(\frac{R}{R_0}\right) = \frac{\sigma_s - \sigma_0}{2\zeta} = 2\beta \qquad \textbf{3.31b}$$

It has to be pointed out that the assumptions made in the beginning are not necessarily fully satisfied in the experimental system. For instance, we assume that the reservoir tension is constant, while it is in fact likely changing over time. As discussed above, the internal structure of the multilamellar reservoir is rather complex, and the formation and accumulation of defects might lead to an increase in reservoir tension over time. Additionally, the spreading coefficient will be affected by the instant inter-bilayer lipid transfer of the membrane through fusion or hemifusion pores. The presence of such pores in double bilayers was investigated and confirmed in Paper V. Another variable parameter is the thickness d of the interbilayer space. This is relevant for the friction coefficient $\zeta = \eta/d$, where η is water viscosity. Local changes in surface roughness or inhomogeneities of the substrate will influence d, which accordingly alters the friction coefficient.

3.8 Modes of lipid transport between bilayer membranes

3.8.1. Inter-bilayer transfer

Lipids can migrate between bilayers across the aqueous phase by i) monomer transfer, ii) transient collision and iii) insertion, a variant of ii)[63]. These direct modes are slow, occurring on the order of minutes. We observed experimentally the rapid transfer of lipids from isolated patches, or islands in the distal (upper) to the proximal (lower) bilayer of a stacked double bilayer on the millisecond timescale (**Figure 3.10**).
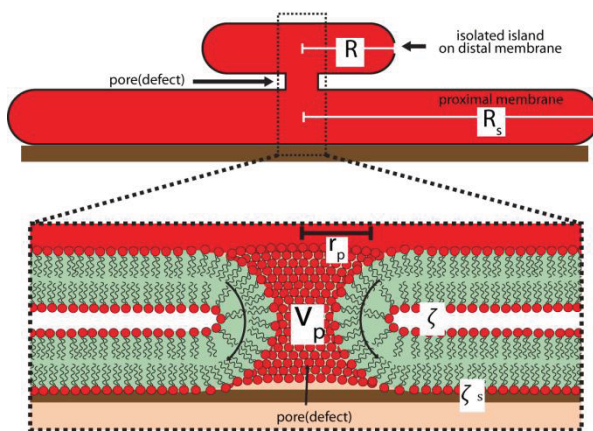
Figure 3.10 Inter-bilayer flow from distal to proximal membrane through a pore(defect).

The study provided evidence that fast transfer of lipids can occur through pores interconnecting two bilayers. Such pores are known to exist in multilamellar reservoirs[58] or form due to tension, shear stress, or protein interactions [64-69]. Isolated islands are patches in the proximal bilayer membrane which were entirely separated from the main distal membrane, such that no connection to the MLV remains. Occasionally, we observed spontaneous tearing of such distal island, but did not find any associated area increase. Instead, we observed an area increase of the proximal bilayer, and concluded that lipid transfer between the bilayers must occur. Direct lipid transfer through the aqueous interlayer, as mentioned above, could be ruled out (Paper V), leaving pore mediated transfer as an alternative.

In this model, we assumed a single circular pore accommodating the flow from an isolated distal membrane island towards the proximal layer, and compared the magnitudes of two modes of dissipation during the transfer. Dissipation is the energy loss due to friction or viscous flow during spontaneous surface free energy optimization of the membrane. One pathway of dissipation is due to the friction between the two stacked membranes, the other one is due to friction at the interface between the substrate and the proximal membrane. While the proximal bilayer is spreading, these two friction regimes will cause some energy loss. The second pathway of dissipation is due to the viscous flow of the membrane, which in the vicinity of the pore could greatly differ from the more remote membrane areas. If the viscous dissipation is at the same order of magnitude or lower than the sliding friction, one pore would be enough for the lipid transfer. On the time scales we observe if the viscous dissipation is higher than the sliding friction, then one pore would not be enough to accommodate the lipid flow.

In the following we compare the viscous (Stokes) dissipation to the dissipation caused by the sliding friction in order to estimate the number of pores needed to accommodate membrane transport. To get a semi-quantitative measure of the dissipation we consider an isolated patch with a single defect connecting to a larger circular patch representing the lower bilayer (**Figure 3.10**). The dissipation ($T\dot{S}$) function for 2D membrane incompressible flow (Stokes flow) is[70]:

$$T\dot{S} = 2\mu \int dA \left(\frac{\partial v_i}{\partial x_k} + \frac{\partial v_k}{\partial x_i} \right)^2 \qquad \textbf{3.32}$$

where v is the membrane velocity and µ is the membrane viscosity, and v_i and v_k are the components of velocity. x_k, x_i are components of position, where i and k change from 1 to 2 in a 2D membrane. If we assume radially symmetric membrane flow, $v = \frac{r_p}{r} v_p$ around a pore, and integrate equation 3.32 from r_p to R, we obtain

$$T\dot{S} = 2\mu \int dr 2\pi r \left[\left(\frac{\partial v}{\partial r} \right)^2 + \left(\frac{v}{r} \right)^2 \right] = 8\pi\mu v_p^2 r_p^2 \int_{r_p}^{R} \frac{dr}{r^3} \approx 4\pi\mu v_p^2 \qquad \textbf{3.33}$$

where v_p is the membrane velocity in the defect. Note that the integral **3.33** converges rapidly, as R increases. This means that the viscous dissipation is concentrated to the pore area.

Taking into account the dissipation on both the proximal and the distal bilayer side of the pore, we obtain

$$T\dot{S} = 8\pi\mu v_p^2 \qquad\qquad \textbf{3.34}$$

The sliding friction dissipation is composed of two parts, the sliding between the upper and lower patch, and the sliding of the lower bilayer on the surface:

$$T\dot{S} = 2\pi\zeta\,(2v_p)^2 r_p^2 \ln\left(\frac{R}{r_p}\right) + 2\pi\zeta_s v_p^2 r_p^2 \ln\left(\frac{R_s}{r_p}\right) \qquad\qquad \textbf{3.35}$$

where ζ is the sliding friction coefficient between the two bilayers, and ζ_s the coefficient between the proximal membrane and surface. R is the radius of the island patch, R_s the radius of the spreading proximal bilayer, and r_p the pore radius (**Figure 3.10**). The 2D membrane viscosity (μ) is on the order of the water viscosity η_w. Note that, in contrast to dissipation caused by the Stokes flow, dissipation due to sliding friction is not very local. In fact, the sliding friction around the pore does not converge, but depends logarithmically on the size of the membrane patch. The membrane sliding friction is not a material constant; its value depends on the amount of water trapped between the bilayers, and the degree of adhesion, respectively. Using experimentally determined values for the membrane dimensions and the flow velocity, and assuming reasonable values for friction coefficients and pore diameter, we found in Paper V that the Stokes dissipation is of the same order or lower than the sliding friction. Hence, the dissipation around a defect is spatially localized and high, but it is not expected to exceed the dissipation of sliding friction of membrane patches, therefore only one pore is necessary to accommodate the rapid lipid transfer.

To support this argument, a characteristic length scale L indicating the relative significance of viscous and frictional forces can be determined. This is similar to the *Reynolds number* in fluid mechanics, a number which determines the ratio of inertial forces to viscous forces, quantifying the relative importance of these two forces for given flow conditions. Low

Reynold numbers represent laminar, high Reynolds numbers turbulent flow. Above the critical length scale the membrane is under the influence of frictional forces. Below it, the viscous forces are more effective.

In the following I present an estimation of the characteristic length scale at which the frictional forces are of the same order as the viscous forces.

$$\nabla\sigma = \zeta\vec{v} - \mu\nabla^2\vec{v} \qquad \textbf{3.36}$$

The first term in **3.36** describes the frictional forces for the supported membrane, while the second term describes the viscous forces. The difference determines the tension gradient in the membrane. I am looking for the length scale, where the frictional forces are of same order as viscous forces:

$$\zeta V \sim \mu\frac{V}{L^2}, \qquad \textbf{3.37}$$

Where V is the characteristic velocity. The cross-over lenght scale is:

$$L_c = \sqrt{\frac{\mu}{\zeta}} \qquad \textbf{3.38}$$

The viscosity μ of the membrane (10^{-3} dyn s cm^{-1})[71] is on the order of the water viscosity η_w (8.9×10^{-3} dyn s cm^{-1}).

The friction coefficient[32] is

$$\zeta = \frac{\eta_w}{d_w} \qquad \textbf{3.39}$$

where d_w is the thickness of the water layer, on which the bilayer is sliding. If we assume that d_w is 1 nm, we obtain a characteristic length of ~30 nm. Above this length scale sliding friction is more important than viscosity. Since the pore size (~10 nm, Paper V) is smaller than 30 nm, the pore vicinity will highly likely be under the influence of the viscous forces; hence it is correct to take the viscosity into account when we consider dissipation.

3.8.2. Bilayer-internal lipid transfer

The formation of pores is not limited to local, nanometer-sized defects. Larger pores are known to be stable for seconds in bilayer membranes[72]. However, the area covered by a pore cannot be infinitively large, since the enlarging pore edge gives rise to an opposing force, known as *pore edge tension γ*. Details on the formation of large area pores, having lateral extents of up to ~100 μm, will be covered in the next chapter. In this section I discuss pathways of lateral lipid migration within a bilayer membrane, as membrane material is re-positioned to close such a pore via bilayer or monolayer sliding. In Paper VI, hypotheses were formulated and tested, involving two intra-bilayer transfer mechanisms of lipids: i) bilayer sliding directly from the MLV towards the pore region (**Figure 3.11 A**), and ii) monolayer sliding from the lower membrane towards the pore region (**Figure 3.11 B**).

When the distal bilayer is directly connected to the lipid reservoir (MLV)(**Figure 3.11 A**), the lipid migration leading to the closure of the pore is most likely occuring by bilayer-on-bilayer spreading from the MLV towards the pore region. In this case the dissipation ($T\dot{S}$) is caused by the bilayer-to-bilayer sliding friction.

$$T\dot{S} = \int dA \frac{1}{2}\zeta v^2 \qquad\qquad \textbf{3.40}$$

With the integration interval from R_p to R_c , where $\dot{R}_p = $ dRp/dt, equation 3.40 will give

$$\int_{R_p}^{R_s} 2\pi r dr \frac{1}{2}\zeta \left(\frac{Rp\dot{R}p}{r}\right)^2 = \pi\zeta r_p^2 \dot{r}_p^2 \ln(\frac{R_c}{r_p}) \qquad\qquad \textbf{3.41}$$

where ζ is the sliding friction coefficient between the distal and the proximal bilayers, v is the velocity of the sliding proximal bilayer, R_c is the cut-off characteristic length scale and comparable to the size of the spread, assuming that the pore is centered.

I use this value instead of R_S because it is difficult to make a calculation for a pore at an arbitrary position in a circular spread since the flow field is not radial. ζ is the friction coefficient between the two bilayers.
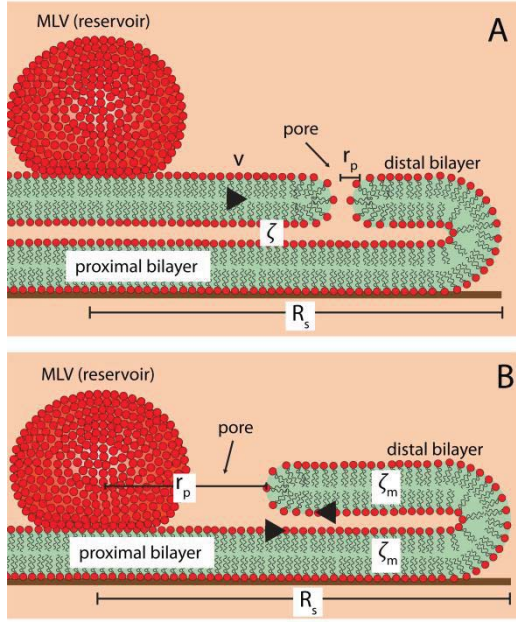
Figure 3.11 Intra-bilayer transfer mechanisms involved in pore closure. *(A) The pore is located on the distal bilayer, there is a connection between the reservoir and the pore region via the distal membrane. (B) The pore is located around the reservoir such that the distal bilayer enclosing the pore has a connection to the reservoir solely via the proximal bilayer.*

The dissipation will be balanced by the edge tension energy (E) of the pore.

$$\dot{E} = 2\pi\gamma\dot{r}_p \qquad\qquad \textbf{3.42}$$

where γ is the pore edge tension and r_p is the pore radius ($\dot{r}_p = \frac{dr_p}{dt}$). The dissipation caused by the bilayer-to-bilayer sliding friction is balanced by the edge tension energy of the pore:

$$T\dot{S} + \dot{E} = 0 \qquad\qquad \textbf{3.43}$$

Inserting equations **3.41** and **3.42** into equation 3.43 will give:

$$\zeta r_p^2 \, \dot{r}_p \, ln(\tfrac{R_c}{r_p}) = -2\gamma \qquad\qquad \textbf{3.44}$$

We can rearrange equation **3.44**:

$$r_p^2 \, \dot{r}_p \, ln(\tfrac{R_s}{r_p}) = -\tfrac{2\gamma}{\zeta} \;\; (\dot{r}_p = \tfrac{dr_p}{dt})$$

$$r_p^2 ln(R_s)\frac{dr_p}{dt} - r_p^2 ln(r_p)\frac{dr_p}{dt} = -\frac{2\gamma}{\zeta}$$

Integrating the left side of equation **3.44** from $r_p=R_p$ (pore radius at t=0, i.e. initial pore radius) to $r_p=0$ and the right side of the equation from 0 to τ (the time required for the pore to relax) gives

$$\int_{R_p}^{0} r_p^2 ln(R_s)dr_p - \int_{R_p}^{0} r_p^2 ln(r_p)dr_p = -\int_{0}^{\tau} dt \frac{2\gamma}{\zeta}$$

$$-\frac{1}{3}R_p{}^3 \ln(R_s) + \frac{1}{3}R_p{}^3 \ln(R_p) - \frac{1}{9}R_p^3 = -\frac{2\gamma}{\zeta}\tau \qquad\qquad \textbf{3.45}$$

Rearranging equation **3.45** and isolating τ from the equation gives

$$-\frac{1}{3}R_p{}^3 \ln\left(\frac{R_s}{R_p}\right) + \frac{1}{9}R_p{}^3 = \frac{2\gamma}{\zeta}\tau$$

$$\tau = \frac{\zeta \, R_p{}^3}{\gamma} \cdot \frac{1}{6}\left[ln(\tfrac{R_s}{R_p}) + \tfrac{1}{3}\right] \sim \frac{\zeta \, R_p{}^3}{\gamma} \qquad\qquad \textbf{3.46}$$

Note that the size of the membrane R_s is only a logarithmic factor. This means τ is only weakly dependent on size of the membrane, but strongly dependent on the size of the pore R_p. With experimental values of r_p, τ and γ from Paper VI, the friction coefficient for the bilayer sliding of the distal bilayer can be calculated as in equation 3.39. This value is then used to determine the water layer thickness for the sliding to make a comparison with earlier reported values[32].

In some instances, the pore surrounds the MLV entirely (**Figure 3.11 B**). In this case the pore can only be repaired by supplying lipid material through the distal bilayer. Since we observed that the perimeter of the proximal bilayer is not changing, it is evident that the vesicle is strongly adhering to the surface. Reverse bilayer rolling to close the pore is therefore unlikely, and lipids would rather be transported to the pore area by monolayer sliding. The

monolayer friction coefficient can be calculated using a dissipation function, similar to equation **3.40**.

$$T\dot{S} = \int_I \, dA \frac{1}{2} \zeta_m v_I^2 + \int_{II} \, dA \frac{1}{2} \zeta_m v_{II}^2 \qquad \textbf{3.47}$$

Indices I and II refer to the surface area of the proximal and distal bilayer, respectively. $T\dot{S}$ is the dissipation due to sliding friction, ζ_m is the coefficient of monolayer sliding friction (sliding friction between the leaflets of the bilayer) and v is velocity of the sliding monolayer.

Using integral intervals for the proximal bilayer from R_L (effective radius of the lipid source, $R_L \sim R_0$) to R_S (radius of the spread), and for the distal bilayer from R_p (pore radius) to R_S with equation **3.47** gives

$$T\dot{S} = \int_{R_L}^{R_S} 2\pi r dr \frac{1}{2} \zeta_m (2\frac{R_p \dot{R}_p}{r})^2 + \int_{R_p}^{R_S} 2\pi r dr \frac{1}{2} \zeta_m (2\frac{R_p \dot{R}_p}{r})^2$$

where $\dot{R}_p = dRp/dt$, and further

$$T\dot{S} = 4\pi \zeta_m R_p^2 \dot{R}_p^2 \ln(\frac{R_S^2}{R_L R_p}) \qquad \textbf{3.48}$$

The (time dependent) line tension energy (E) of a pore is:

$$\dot{E} = 2\pi \gamma \dot{R}_p \qquad \textbf{3.49}$$

where γ is pore edge tension. Equating 3.48 with 3.49 ($T\dot{S} = \dot{E}$) gives

$$2\frac{\zeta_m \, R_p^2}{\gamma} \dot{R}_p \ln(\frac{R_S^2}{R_L R_p}) = 1 \qquad \textbf{3.50}$$

The friction coefficient of a sliding monolayer was calculated from equation 3.50 (Paper VI) to be 10^5 to 10^6 Ns/m. Typical values for inter-leaflet monolayer friction coefficients have been reported as 10^8 to 10^9 Ns/m[73-74]. Simulations have shown that ζ_m can in some circumstances be situated in the area of 10^6 Ns/m, so we do not rule out monolayer friction as a transport mechanism.

3.9 Lipid nanotubes

Lipid nanotubes are peculiar, high-aspect ratio embodiments of bilayer membranes (**Figure 3.12 A**). They are hollow cylindrical membrane structures with diameters of only ~ 100 nm, but can reach a length of hundreds of micrometers. Membrane nanotubes are commonly observed in cell cultures in vitro, where their individual properties are rather heterogeneous. Little is known about their role in vivo. It was only recently discovered that membrane nanotubes form transient connections between individual cells, and can possibly facilitate intercellular communication[75]. Accordingly, investigation of their basic physical and chemical properties, their function in vivo, and their fabrication and application in man-made biomimetic systems are of growing interest. In Paper II we report a new contact-free fabrication technique for nanotubes, and in Paper III we studied the nanoparticle-induced formation of lipid nanotubes from double bilayer patches. Membrane nanotubes are known to form spontaneously from and between biological cells, but it remains a challenge to understand the formation mechanism, and how long-range material and information interchange occurs via nanotubes.

For a lipid nanotube, the Helfrich curvature energy (**3.2**) is written as:

$$F_{nanotube} = \int dA [\frac{\kappa}{2}(c_1 + c_2 - c_0)^2 + \sigma]$$

Integrating equation **3.2** (without spontaneous curvature c_0) gives F as a function of the nanotube radius r and length l:

$$F_{nanotube} = \frac{\kappa}{2}\frac{1}{r^2} 2\pi r l + \sigma 2\pi r l = 2\pi r l \left(\frac{\kappa}{2r^2} + \sigma\right) \qquad \textbf{3.51}$$

The surface energy of the nanotube per unit length $f_{nanotube}$ is thus

$$f_{nanotube} = 2\pi r \left(\frac{\kappa}{2r^2} + \sigma\right) \qquad \textbf{3.52}$$

If we minimize the energy of equation, **3.52** with respect to r, an equilibrium tube radius will be determined as:

Figure 3.12 Phospholipid nanotubes.

(A) A section of a phospholipid nanotube. The tube wall is a curved single bilayer. (B) A flat phospholipid bilayer membrane with slightly curved particles adhering to one of the two monolayer leaflets. The membrane bends along the curve of the particles. (C) A cylindrical nanotube emerging from a flat membrane. The neck where the nanotube connects to the membrane features a high curvature (inset).
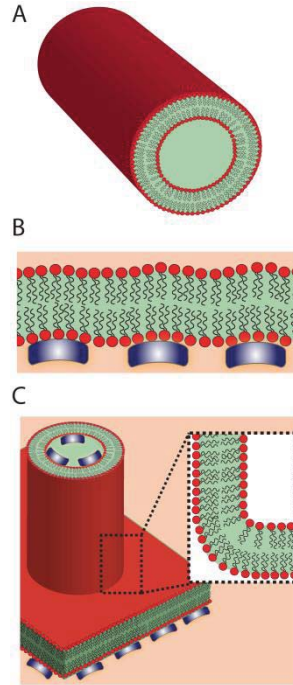
$$r_{eq} = \sqrt{\frac{\kappa}{2\sigma}}$$

3.53

Equation **3.53** implies that the radius of a tube is a force balance between the bending modulus and the vesicle surface tension.

So far we have neglected the spontaneous curvature c_o in Equation **3.2**. The spontaneous curvature accounts for the asymmetry between the monolayer leaflets of the membrane, for example in case of structural differences between the lipids in each leaflet. Increasing the spontaneous curvature will reduce the surface free energy and favor tube formation. In Paper III, we show experimental evidence, and argue that if one leaflet of the monolayer is invaded by nanoparticles with slightly curved morphology (**Figure 3.12 B or C**), lipid nanotubes spontaneously form.

A theoretical model in which nanotube formation in cell membranes was induced by the adhesion of small protein aggregates was previously

presented by Ewers[76]. According to this model, which couples the thermodynamics of phase separation to the mechanics of membrane deformation, tubulation is governed by the free energy difference (ΔF_N) between the particle-adhered flat membrane and particle-adhered tubes. The energy difference (ΔF_N) in the model refers to the energy difference between these two bound states.

$$\Delta F_N = E_{neck} - N(kT\ log\phi_1 + \Delta e) \qquad\qquad \textbf{3.54}$$

where, E_{neck} is the energy of the toroidal neck connecting the tubule to the membrane, N is the number of particles, Δe is the energy gain and $kT\ log\phi_1$ is the entropy loss, when the particles migrate from the flat membrane into the tubule. ϕ_1 is the surface fraction, which is defined as the product of concentration and area of the particles on the membrane, and kT is the thermal energy (2.5 kJ/mol). I mentioned earlier in section **3.3 Membrane mechanics** the relation between the free energy and the bending energy of the lipid membranes. If slightly curved particles adhere to a flat bilayer membrane, the membrane will bend along the particle curvature (**Figure 3.12 B**), which increases the bending energy of the membrane, compared to the particle-free flat membrane. When tubulation occurs, the particles that are adhered to the planar membrane migrate into the tubes (**Figure 3.12 C**). On one hand, since the tubes already have highly curved side walls, there will be a gain in energy (Δe) for the particle-adhered planar membrane if it joins a tube. On the other hand, an increasing number of adhering particles will also cause a loss of entropy. On the flat membrane particles can diffuse freely, but inside the tube they will switch to a more ordered arrangement. This will cause a decrease in entropy which in turn increases the free energy of the system. The term $kT\ log\phi_1$ refers to this entropic loss. The energy gain has to overcome the entropy loss to favor tube formation. Note that when tube formation occurs, the curvature at the interface where the tube connects to the planar membrane (a toroidal neck) will be high (inset in **Figure 3.12 C**), which requires energy (E_{neck}). Even though tube formation is favored with increasing number of particles N, a critical number of particles N_c has to accumulate to reach this barrier.

In 2012, Saric et al.[77] cited Paper III in a report, in which the results of Monte Carlo simulations confirmed the effect of colloidal particles on nanotube formation. The study shows that adhering particles produce the nucleation

seeds for tubulation by lowering the free energy barrier, as predicted by the model of Ewers et al.[76].

In Paper III we briefly considered the possibility of nanotube formation by hydrodynamic drag as an alternative tubulation mechanism. Thermal convection caused by water evaporation from the open observation cell could exert a force on the membrane of the FGUV. The hydrodynamic drag force on a nanotube is $F = \zeta_{\parallel} v L$ with friction coefficient $\zeta_{\parallel} = \frac{2\pi\eta}{ln(L/r)}$, where η is the water viscosity, L is the tube length and r the tube radius. The flow velocity around a nanotube (v) was estimated from the velocity of nearby free-floating vesicles. For sufficiently long tubes, the drag force is expected to overcome the critical force f_c (~ 10 pN[78]) needed for mechanical tube extrusion. The critical length, which is the length required for hydrodynamic drag to contribute to tube elongation, is $L_c = \frac{f_c}{\zeta_{\parallel} V}$. L_c was calculated to be 4 mm, which is much larger than the observed tube length in any of the experiments.

# Chapter 4 : NON-TRIVIAL RUPTURE MECHANICS

4.1 Membrane ruptures

Plasma membrane ruptures, e.g., the forceful opening of large area pores, is a widespread form of biological cell damage. Even under normal physiologic conditions *in vivo*, up to 20-25% of mammalian skeletal and cardiac muscle cells and 6% of skin cells are in a damaged state due to stretching and shearing[79-80]. Moreover, irreversible rupture of muscle and cardiac muscle cell membranes (due to the lack of the membrane supportive protein dystrophin) leads to muscular dystrophy, an incapacitating disease[81-82]. In addition to causing health concerns, controlled rupture, or pore, formation in plasma membranes is of importance for advanced medical applications such as gene therapy[83-84] and drug delivery[85-86].

Incisions in lipid membranes can occur as a result of exposure to chemical agents, for example, detergents[87], proteins[88], cationic lipid particles[89], or due to intrusive physical procedures like electroporation[45], osmotic stress[90], ultrasound[86] and strong adhesion to substrates[72,91].

Before we discovered two new rupture modes in lipid bilayers (Paper IV), [92], only circular pores were known to form in biological membranes, as pore edge tension γ favors circularly shaped pores[44,72,93-94]. When a pore opens in a lipid membrane under lateral tension (σ), the energy per membrane unit area is reduced proportionally to the pore area. For example, by nucleation of a circular pore radius r_p in the membrane, the energy reduction will be: $-\sigma\pi r_p{}^2$. This drop in energy will be opposed by the pore edge tension, which is proportional to the pore perimeter. For a circular pore, the opposing energy is $2\pi r_p\gamma$. The total energy E of the pore is therefore

$$E = 2\pi r_p\gamma - \sigma\pi r_p{}^2 \qquad\qquad \textbf{4.1}$$

Figure 4.1. depicts the relationship between the pore energy and the pore radius r_p, at constant membrane and pore edge tension. Initially, when the pore nucleates in the membrane, there will not be a gain in free energy. This is due to pore edge tension, which counteracts the growth of the small pore. When the pore reaches a critical size r_c the energy gain due to the reduction of membrane tension outgrows the energy loss due to growing pore edge tension. Membrane tension is reduced by the area gain of the pore.

$$r_c = \frac{\gamma}{\sigma}$$
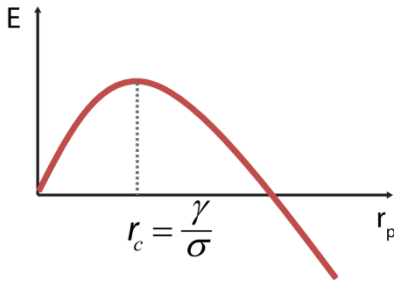
Figure 4.1. Total energy of a pore(E) as a function of pore radius(r_p). *At a constant membrane (σ) and pore edge tension (γ), the pore initially (right after nucleation) loses energy, due to the pore edge tension. Above a critical radius (r_c), the membrane tension overcome the opposing edge tension. In practice, the membrane ruptures when $r_c \sim nm$, i.e, $\sigma \sim \gamma/nm$.*

Above r_c, the pore will grow.

It is reasonable to assume that a pore will tend to adapt a shape where the pore area is maximal and the perimeter is minimal, to provide the largest energy reduction for the membrane. Among 2D geometries, the area to perimeter ratio is maximal in a circle. Therefore circular pores are energetically the most favorable.

In free standing vesicles, tension will be gradually reduced after opening of a pore, due to equilibration of osmotic pressure. In supported membranes tension is caused by surface adhesion and remains constant after opening of a pore. This can lead to large pores in supported membranes or FGUVs.

In Paper IV we have reported two types of irregular pore morphologies in biological membranes. **Figure 4.2**. shows the new membrane ruptures we observed, which exhibit two distinct pore shape patterns: floral (**Figure 4.2. A**) and fractal (**Figure 4.2. B**). These patterns highly resemble those observed in 'viscous fingering'; a phenomenon which is observed during flow in porous media. In the next chapter I will introduce the concept of viscous fingering and lay out the analogy of dynamics of membrane ruptures to the dynamics of this phenomenon.
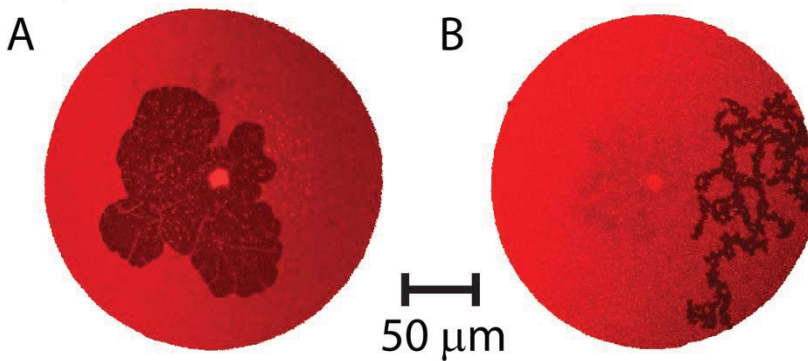
Figure 4.2. Irregular pore morphologies. *Confocal fluorescence micrographs of supported double bilayers (top view) featuring (A) a rupture of floral and (B) of fractal morphology.*

4.2 Viscous fingering in porous media

If in a porous medium, such as packed microparticles within a fluidic confinement, a second fluid of lower viscosity is forced through the particle bed to displace the first fluid, a morphologically instable interface of these two immiscible fluids results. This instability is known as 'viscous fingering'[95], since the boundary displays very typical, complex fingering patterns. These patterns strongly resemble the membrane ruptures we observe (**Figure 4.2**). Porous media are abundant in nature; examples are soil, zeolites, and also biological materials such as bones, wood, and cork. A number of man-made products such as cements and ceramics are also considered as porous media. Viscous fingering is in the focus of several important technical applications, for example oil recovery[96], fluid mixing[97], soil physics[98], and biological tissue and organ engineering[99-100].

Interfaces of fluids are known to exhibit instabilities[18]. Membranes are also (two-dimensional) fluids, and it is conceivable that the membrane flow can cause edge instabilities. Here I show that in addition to the similarity of patterns there is a direct mathematical analogy of the equations used to describe the dynamics of viscous fingering and the rupturing of biological membranes (Paper IV).

The flow dynamics of a fluid bilayer membrane sliding over a supported (and therefore immobile) membrane is described by the local force balance (**3.13**):

$$\vec{v} = \nabla\sigma$$

This is in fact the same as the *Hele-Shaw* equation, a form of the Darcy equation which is used to describe a Hele-Shaw flow. A Hele-Shaw cell is a specific experimental set up which simulates in 2D the flow in 3D porous media[101] (**Figure 4.3 A**).
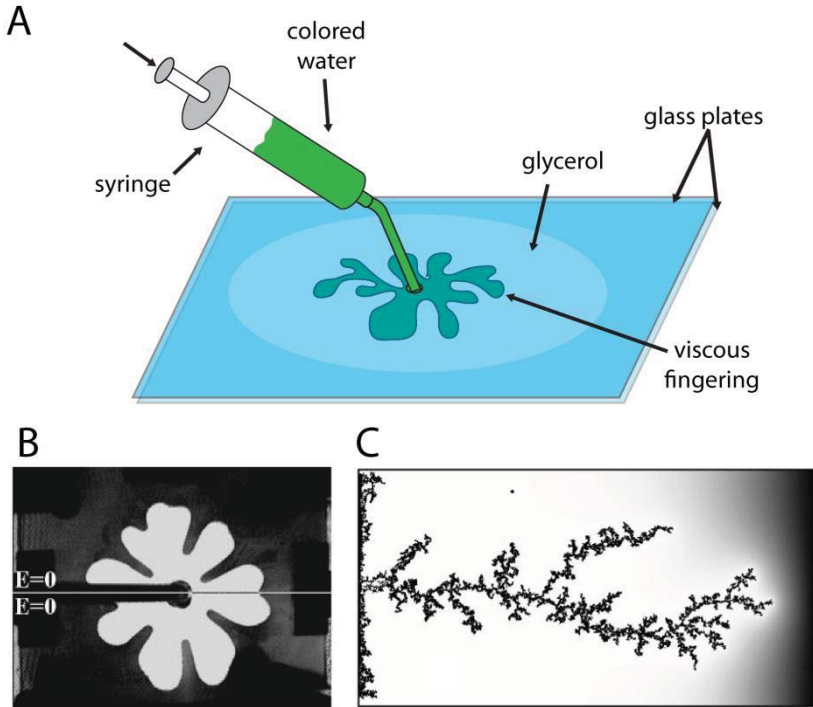
Figure 4.3 Hele-Shaw Cell. *(A) Experimental set-up of a Hele-Shaw cell. Two glass plates are placed on top of each other, separated by a small distance, and a tiny injection port in the upper plate. Glycerol, a highly viscous fluid is injected first, depicted by the circular white area in the blue cell. Subsequently, a less viscous liquid, such as water, depicted in green, is injected. The injection causes viscous fingering patterns. (B) Images of Saffman-Taylor Instabilities by Toth-Katona et al.[102] and (C) Invasion Percolation Clusters by Lovoll et al.[103] from actual experiments. For (B) a liquid-crystalline substance doped with a dye was used as a defending fluid. Air was used as an invader. For (C) the defending liquid is 90%–10% by weight glycerol-water solution dyed with 0.1% Negrosine to increase the contrast between the colored fluid and the invader (air). Note that in Experiment C, the inlet is not in the center of the plates, but on the left side. Images in (B) and (C) are reproduced by permission, © American Physical Society.*

The cell consists of two parallel flat glass plates separated with an infinitesimally small distance h. If h is small, the incompressible flow ($\nabla \vec{v} = 0$) inside will be laminar at all velocities.

A Hele-Shaw flow is a 2D form of Darcy flow defined as below:

$$\vec{v} = -\frac{h^2}{12\mu}\nabla P \qquad \qquad \text{4.2}$$

where $\vec{v}$ is the velocity field. In fluid dynamics, this vector mathematically describes the motion of the fluid, and the length of the vector field is the flow speed. h is the distance between the two plates, μ is the viscosity of the fluid and ∇P is the pressure gradient.

At the moving boundary of a fluid in the Hele-Shaw flow, the inviscid edge is balanced by the pressure of the invading liquid:

$$P = -\gamma c \qquad \qquad \text{4.3}$$

where P is the pressure, γ is the surface tension, and c is edge curvature. The membrane is in a first degree of approximation also incompressible ($\nabla \vec{v} = 0$). At the boundary of a rupture, or membrane pore, the membrane tension σ balances the line tension stress γ:

$$\sigma = \gamma c \qquad \qquad \text{4.4}$$

where c is the edge curvature of the rupture. The instability of a pore edge, with the pore void representing an inviscid fluid, can therefore be considered equivalent to a Saffman-Taylor instability[104] occurring at the interface of two fluids in a Hele-Shaw cell (**Figure 4.2 A** and **Figure 4.3 B**). **Table 4-1**. summarizes the analogies between membrane flow properties and the Saffman-Taylor instabilities.

In a plain Hele-Shaw cell the porosity is regular. By inserting grains (for example glass beads[101]) randomly, it is possible to create inhomogeneous porosity, leading to irregular permeability. In this case the capillary forces are more effective and cause displacements with fractal morphology.

Table 4-1. Analogies between membrane flow and the Saffman-Taylor instabilities.

| Membrane flow	Saffman-Taylor instability
$\zeta\vec{v} = \nabla\sigma$	$-\dfrac{12\mu}{h^2}\vec{v} = \nabla P$
$\nabla\vec{v}=0$	$\nabla\vec{v}=0$
$\sigma = \dfrac{\gamma}{R}$	$P = -\dfrac{\gamma}{R}$

The appearance of fractal displacements[101,105] (**Figure 4.3 C**) is different than in Saffman-Taylor type of fingering[104,106] (**Figure 4.3 B**) in which the viscous forces are dominant. These fractal form of displacements resemble invasion percolation clusters[103,105,107] where the invading fluid chooses the `path of least resistance', taking the shape of a percolation cluster that entraps islands of the displaced fluid. The invasion occurs in characteristic burst, know as Haines jumps[108]. Percolation does not require fluid injection. Invasion of a highly viscous fluid by a fluid with lower viscosity can be also observed during the drainage of a less viscous fluid (air) through a fluid with higher viscosity (water)[108] which is one of the common setups for invasion percolation experiments.

It is not necessarily easy to understand why a lipid membrane flow upon rupturing would follow flow dynamics of a porous medium. During the formation of floral ruptures (**Figure 4.2 A**) (Saffman-Taylor analogous), thin threads of membrane, which are indicators for membrane-surface pinning, were consistently observed at the pore edge. Pinning can contribute to the instability of the floral pores (Paper IV). Roiter et al. have shown by means of atomic force microscopy (AFM) how particles of ~20 nm diameter create incisions in supported membranes[109]. The AFM scans of the SiO_2 surfaces in Paper II and VI have revealed the presence of grains of comparable dimension. Pinning of parts of the distal bilayer to such grains by means of Ca^{2+} ions would locally reduce the fluidity of the membrane. The flow of lipids during a rupture event can essentially be viewed as flow through a two-dimensional porous medium, where fluid membrane interacts with immobile areas. This percolation dynamics could equally arise from Ca^{2+}-mediated pinning points between the bilayers[62].

Invasion percolation dynamics also occurs in avalanches with broad size distribution. Briefly, avalanches are sudden increases in the response of a system to stress. Both the patterns of fractal ruptures (**Figure 4.2 B**) with trapped membrane islands, and the avalanche statistics are consistent with invasion percolation dynamics observed in fluid displacement experiments. In addition, the fractal dimension (*c.f.* **4.3 Fractals & fractal dimension**) of the fractal ruptures, D =1.71, is lower than the theoretical value, D=1.83, but comparable to typical values of invasion percolation clusters[110-111].

We have not yet been able to provide a clearly defined analogy between the fractal ruptures and the invasion percolation instability, as we did for floral ruptures with respect to Saffman-Taylor instabilities. However, it is possible to determine a characteristic length scale for membrane pores, in which they are not expected to exhibit instabilities.

The time scale to relax a pore shape modulation (τ) follows a simple scaling argument. It is known that in a free-standing vesicle, pore flow dynamics is governed by the membrane viscosity (μ)[72]. Consider a periodic membrane edge modulation u = ε (t)sin (qx). The wavelength L and peak amplitude ε of this modulation is depicted in **Figure 4.4**.
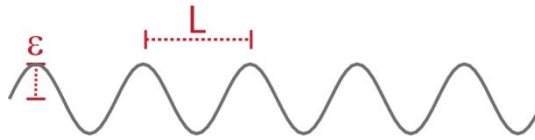
Figure 4.4 A periodic membrane edge modulation with wavelength L and amplitude A.

The excess energy compared to a straight edge (u=0) over one wavelength is

$$E = \gamma \int_0^L dx \left(\sqrt{1 + \left(\frac{du}{dx}\right)^2} - 1 \right) \approx \gamma \int_0^L dx \frac{1}{2}\left(\frac{du}{dx}\right)^2 = \pi^2 \gamma \frac{\varepsilon^2}{L} \qquad \textbf{4.5}$$

The edge modulation will normally relax to produce a straight edge, but it will take some time due to dissipation. In a free standing membrane the dissipation comes from the 2D Stokes flow of surfactants in the membrane (Equation **3.32**):

$$T\dot{S} = 2\mu \int dA \left(\frac{\partial v_i}{\partial x_k} + \frac{\partial v_k}{\partial x_i} \right)^2$$

We integrate over one wavelength L, the dissipation scales as

$$T\dot{S} \sim \mu \, L^2 \left(\frac{V}{L} \right)^2 \sim \mu V^2 \sim \mu \dot{\varepsilon}^2 \qquad\qquad \textbf{4.6}$$

Balancing the excess edge energy with dissipation gives equation **3.43**:

$$T\dot{S} + \dot{E} = 0$$

from which (on a scaling level) the relaxation time can be determined:

$$\dot{\varepsilon} \sim -\frac{1}{\tau} \varepsilon \qquad\qquad \textbf{4.7}$$

where the relaxation time is

$$\tau \sim \frac{\mu}{\gamma} L \qquad\qquad \textbf{4.8}$$

In a supported membrane this timescale is much longer, and increases rapidly with the wavelength of the modulation: the dissipation due to sliding friction (calculated over one wavelength) scales as (**3.40**):

$$T\dot{S} = \int dA \frac{1}{2} \zeta v^2 \sim \zeta L^2 V^2$$

Balancing dissipation and energy gain (as above for **3.42**) gives:

$$\tau \sim \frac{\zeta}{\gamma} L^3 \qquad\qquad \textbf{4.9}$$

where ζ is the friction coefficient between the proximal and the distal bilayers.

A rupture propagating at velocity v exposes a membrane edge length L in time τ:

$$\tau = \frac{L}{v}$$

    4.10

Equating **4.9** and **4.10** gives a characteristic length (L_c):

$$L_c = \sqrt{\frac{\gamma}{\zeta v}}$$

    4.11

For modulations larger than L_c, the relaxation of edge shape modulation will take more time than the rupture process itself. This leads to the possibility of an unstable edge. When the values we estimate from the time series of the rupturing membrane in Figure 3 of Paper IV are introduced into this equation, we obtain a characteristic length (L_c) ~0.1 μm.

4.3 Fractals & fractal dimension

"Why is geometry often described as 'cold' and 'dry?' One reason lies in its inability to describe the shape of a cloud, a mountain, coastline, or a tree. Clouds are not spheres; mountains are not cones, coastlines are not circles, and bark is not smooth, nor does lightning travel in a straight line." Benoit Mandelbrot, the father of fractal geometry (1924-2010)[112].

Fractals are complex patterns which are self-repeating regardless of magnification. For example, any branch of a tree will resemble the entire tree. Clouds, lightening, snowflakes, mountain ranges, branching pattern of rivers, broccoli, fern, butterfly wings[113], the bronchopulmonary system[114], bacterial growth patterns[115], self assembled proteins[116], the structure of chromosomes[117] and DNA sequences[118] are other examples of fractals in nature. In the field of lipid membrane research, membrane domains as well as the growth patterns of liposomal aggregates[119] or spreading films[30] have been shown to exhibit fractal patterns[120-121].

The development of fractal geometries in nature offers distinct advantages to the organisms. A notable advantage of the fractal morphology of some internal organs of mammals is the efficient use of genetic material, saving additional code for every single sub-structure[122]. In physiology, fractal passages of airways in lungs have been shown to provide the maximum

possible surface area for gas and nutrition exchange at the smallest occupied volume[114], and minimum transport distance [123]. Furthermore, the fractal morphology of these structures has been interpreted as an evolutionary benefit, providing the organism with advantages such as greater error tolerance and adaptability[124].

Fractal analysis is the determination of the fractal characteristics of data. It comprises methods to assign a fractal dimension and other characteristics to data which originate either from a model dataset, or is obtained from natural or technical phenomena. The time lines of weather patterns, and ocean temperatures, also of sleep apnea[125] and of the stock exchange[124] are examples of phenomena that exhibit statistical self-similarity.

A fractal dimension is an index, quantifying the complexity of a fractal pattern as a ratio of *change in detail* to *change in scale*[112]. In other words, the fractal dimension describes how an object fills vacant space over different scales. The fractal dimension of a geometric object is an integer, but for a fractal object it is a fractional value (*fractal*). The topological dimensions in regular (Euclidean) geometry are defined such that a point has a dimension of zero, a line has a dimension of 1, a plane has a dimension of 2 and a cube has a dimension of 3. These dimensions, however, are not sufficient to define for example a line with a complexity, e.g., a line which has a kink or many kinks in it. If we divide a straight line into 3 equal segments, each segment is a miniature of the entire object (the line), and each segment has a length which is 1/3 of the original object. The regular dimension (D) is defined as below:

$$N = S^D \qquad\qquad \textbf{4.12}$$

where N is number of segments and S is scale of each segment. For a segmented straight line, N=3 and S=1/3 therefore, the regular dimension of a straight line will be:

$$D = \left|\frac{\log N}{\log S}\right| = \left|\frac{\log 3}{\log(\frac{1}{3})}\right| = 1 \qquad\qquad \textbf{4.13}$$

The result will not change if N increases. The number of segments and the scale will be proportional; therefore the dimension will always be 1.

In **Figure 4.5**, a line of higher complexity is illustrated. This line is a part of the "Koch snowflake"[126], named after the Swedish mathematician Helge von Koch, who first conceived this structure. A dimension D = 1 will not exactly define the Koch curve in **Figure 4.5**, even though it is a line and not a plane. Fractal geometry, a non-conventional geometry, can define an intermediate dimension between a line and a plane, assuming a fractal dimension of non-integer value.
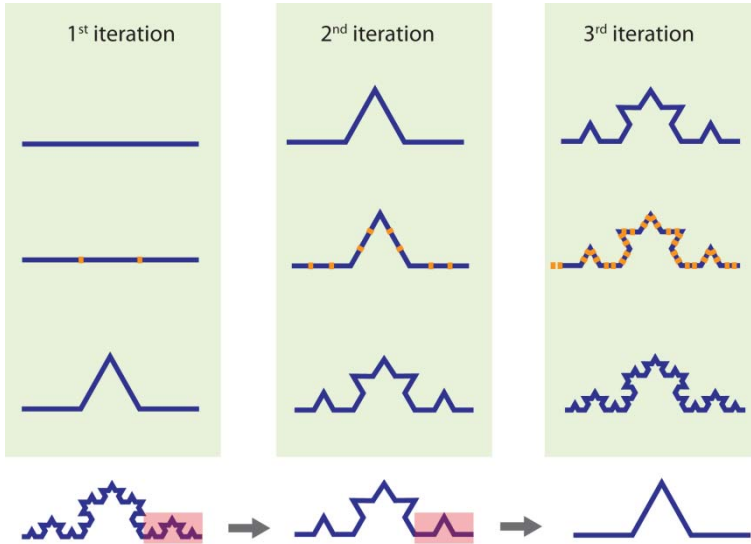
Figure 4.5 Fractal dimension of a Koch curve. *First a straight line is divided into 3 equal segments. The middle segment is deleted and has been transformed into a triangular kink. This division is iterated on each new segment 3 times. The final state consists of 4 segments, each of which is a product of earlier iterations (bottom panels).*

To illustrate the determination of the fractal dimension of the Koch curve, it is created from a straight line and then divided into 3 segments of equal length. The middle segment is deleted, and two segments with a joint connection point, forming the top of a triangle, are drawn (first iteration). For each segment this procedure can be iterated.

For the Koch curve in **Figure 4.5**, the final state of each iteration will have 4 segments (N=4) each of them a replica of the original segment, but of reduced size. The length of each segment will be 1/3 of the precursor length

(S=1/3). Therefore, the fractal (non-integer) dimension of the Koch curve will be (**4.13**):

$$D = \frac{\log N}{\log S} = \frac{\log 4}{\log(\frac{1}{3})} = 1.231$$

There are different methods to determine the fractal dimension[127], each of them most suitable for a specific set of problems. We used the box-counting method [128] in Paper IV to determine the fractal dimension of membrane rupture areas from an acquired image of the fracture. Box counting was performed by placing the fractal image into a grid (a plane divided into "boxes") consisting of an array of squares of equal size. The boxes completely occupied by the fracture area were counted. Afterwards the box size in the grid was decreased, and the number of fully filled boxes was counted again. The fractal dimension is a measure based on the relation between the change in the number of the boxes which are occupied (filled with a fraction) and the box size.

Imagine that the object is a 1 dimensional unit line. If we cover this line with smallest number of boxes N which has a side length dimension of δ, then the relation between N and δ will be $N(\delta) = \frac{1}{\delta}$ If the object is a 2-dimensional unit square we expect $N(\delta) = (\frac{1}{\delta})^2$. Similarly, if it is a 3-dimensional unit cube, $N(\delta) = (\frac{1}{\delta})^3$. It is not a coincidence that the number of dimensions becomes the power of such a relation. For more complex fractal shapes, a power law $N(\delta) = k(\frac{1}{\delta})^D$ can be helpful to establish a relation between N(δ) and 1/δ.

In order to obtain D I take

$$\log N(\delta) = \log \left[k \left(\frac{1}{\delta} \right)^D \right] \qquad\qquad \textbf{4.14}$$

and re-arrange equation **4.14**:

$$\log N(\delta) = \log k + D \log \frac{1}{\delta}$$

$$\frac{\log N(\delta)}{\log \frac{1}{\delta}} = \frac{\log k}{\log \frac{1}{\delta}} + \frac{D \log \frac{1}{\delta}}{\log \frac{1}{\delta}}$$

Solving **4.14** leads to

$$D = \lim_{\delta \to 0} \frac{\log N(\delta)}{\log \left(\frac{1}{\delta}\right)} - \lim_{\delta \to 0} \frac{\log k}{\log \frac{1}{\delta}} \qquad \textbf{4.15}$$

If δ becomes successively smaller, the approximation will greatly improve. If δ is approaching 0, $\frac{1}{\delta} = \infty$, log ∞ →∞, and term $\frac{\log k}{\log \frac{1}{\delta}} \to 0$. D will remain as

$$D = \lim_{\delta \to 0} \frac{\log N(\delta)}{\log \left(\frac{1}{\delta}\right)} \qquad \textbf{4.16}$$

If such a limit exists, it will be the box-counting dimension of the fractal[129]. Limit **4.16** converges very slowly, thus a more practical approach is a logarithmic regression, using a log/log plot of $N(\delta)$ vs. $\frac{1}{\delta}$, which should yield a straight line with slope D and y-intercept $log\,(k)$[130]. This approach was used in Paper IV to obtain the fractal dimension of rupture areas in the distal bilayer of the FGUVs.

4.4 Avalanches and crackling noise

The dynamics of complex systems often occurs in terms of avalanches, rather than following a smooth gradual path. An avalanche is a sudden response of a system to a slowly applied stress. The name 'avalanche' (but not the dynamics!) originates from a snow slide phenomenon observed in nature.

Crackling noise arises when a system responds to a slowly applied external force through discrete, burst-like events, spanning a broad range of sizes[131]. In other words, crackling noise events appear intermittently and each of them has a different magnitude [132]. A typical example is earthquakes: the response of tectonic earth plates to the frictional stress. If the magnitude of earthquakes in a region of the world could be in some way recorded over many years, and played as an audio signal with 10 million times accelerated speed, it would sound much like the sound generated by the slow crumpling of paper, or the noise generated by a burning log of wood, which are two other typical examples of crackling noise. Other examples are the failure of mesoporous materials under compression[133], the reorientation of magnets in a changing magnetic field[131], or front dynamics of adhesive tapes[134]. Not all

systems under tension crackle. Sethna *et al.*[131] explain the distinction of crackling noise from other responses to changing external conditions with two distinct examples: One is the popping of pop-corn when it is heated. The elements (the pop-corn bits) of the system respond individually with similar strength. The other is the snapping of chalk when it is mechanically stressed. Here, the grains of the chalk are very strongly connected; they respond to external stress all together at once. The peculiarity of systems which exhibit crackling noise dynamics is that they are consisting of individual elements which are connecting to each other stronger than the pop corns and weaker than the grains of chalk. This intermediate level of connection present in those systems results in a wide distribution of distinct burst sizes, displaying crackling noise dynamics. The complete understanding of crackling noise has still not been achieved. Deeper insights would, besides describing a fundamental physical concept in the world around us, probably help with practical problems, predicting earthquakes, or the dynamics of the stock markets.

Here I present an unpublished analysis based on fluorescence intensity measurements of the confocal micrograph series of the rupturing lipid membrane in Figure 3 of Paper IV (**Figure 4.6**). The analysis reveals that the fractal avalanche ruptures of the model phospholipid membranes are exhibiting crackling noise dynamics, in analogy to seismological phenomena (**Figure 4.6 B and F**). The data not only exhibit crackling noise characteristics, but also follow the Gutenberg-Richter law known from seismology, which characterizes the abundance and magnitudes of earthquakes[135]: The number of earthquakes N_S with a magnitude S in a defined region over a sufficiently long period of time decreases with increasing values of S according to $N_s \propto S^{-b}$, $\mathrm{Log}\ N_s \propto -b\ \mathrm{Log}\ S$. In other words, among a distribution of sizes of earthquakes over time belonging to a specific region, the big ones will be rare, and the small ones will be frequent.
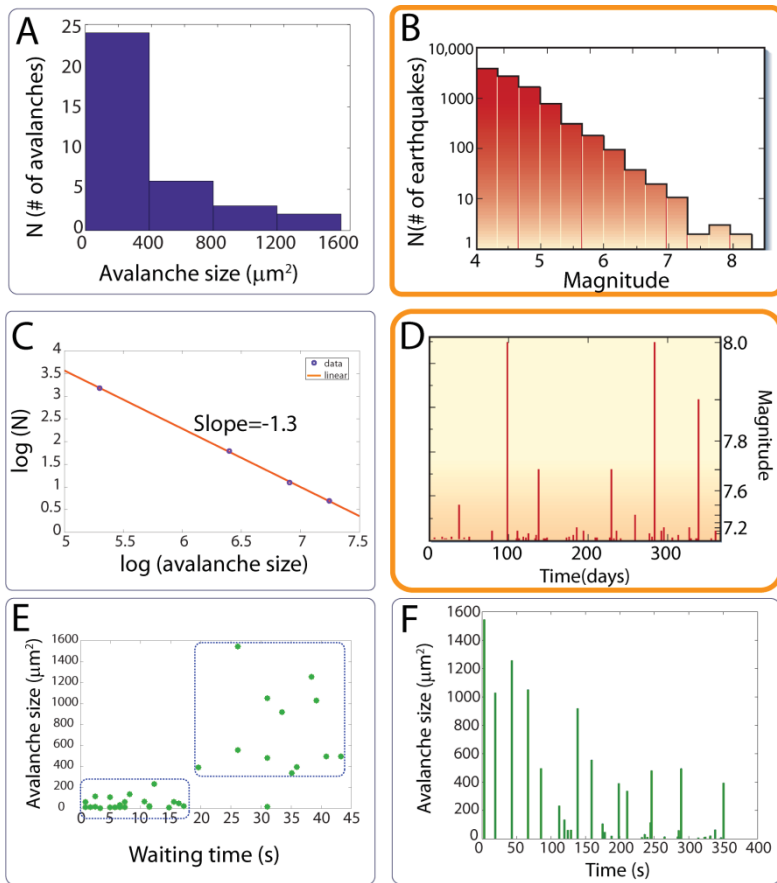
Figure 4.6 Avalanche rupture statistics of double bilayer membranes. *The data is taken from Figure 3 of* Paper IV *(A) Histogram showing the number of avalanche ruptures (N) versus avalanche size. (B) Histogram showing the frequency of the earthquakes (N) versus earthquake magnitude. (C) Log/log plot of data points in (A). These analyses reveal that the biomembrane ruptures follow the Gutenberg-Richter Law of earthquakes: the power law formulating the inverse relation between the frequency and the size of the earthquakes. (D) The plot of earthquake magnitude versus time. (E) Plot showing the avalanche size versus waiting time before the next avalanche. Please note the strong correlation between the avalanche size and the waiting time before the next avalanche (regions marked with dashed lines). (F) Plot of rupture avalanche size versus time. Spikes represent a wide variety of avalanche sizes appearing over time in an intermittent manner, featuring crackling noise dynamics. Note the resemblance to (D). Panel (B) and (D) have been adapted from Sethna et al.[131]. Reproduced with permission, © 2001 Nature Publishing Group.*

Chapter 5 : ARTIFICAL CELL CONCEPTS

""What I cannot create, I do not understand"

Richard Feynman, Physicist (1918-1988) (as quoted in The Universe in a Nutshell by Stephen Hawking)

The first embodiment of the idea of an artificial cell is nearly 50 years old[136]. From the point of view of synthetic biology[137], the definition of the artificial cell (or artificial life in its smallest unit) is rather ambitious, containing a dozen challenging requirements, including self-assembly of a boundary from simple molecules, the ability to capture and transform energy, self-sustained production of catalysts, and error correction during replication. These requirements can currently not be met; to build an artificial cell by these criteria is technically not feasible[138]. However, one can relax the criteria and look at the artificial cell from a more practical perspective, defining the artificial cell as a cell-sized particle, which is created in the laboratory in order to mimic certain functions of the living cell[8,139]. Until today, the majority of engineering approaches to an artificial cell have produced exactly this: packages which are able to mimic certain structural or functional aspects of the biological cell. A term used to describe this kind of approach is the protocell[7-8,10,140-142], or hypothetical precursors of the first biological cells. Protocells consist of chemical components which do not require living content. Another practical term, the minimal cell[143-144], represents a model with the smallest possible genome. This minimal cell should maintain basic metabolic functions and replicate, similar to symbiotic single cell organisms which do not have to synthesize all their own nutrients.

Contemporary artificial cell research primarily aims for a detailed understanding of how the cell works. On the way towards such a minimal cell model, interesting conclusions can be drawn. For example, a study in 2004 by Chen *et al.*[145] has shown that RNA, simply placed in a fatty acid vesicle, creates an osmotic pressure along the membrane by RNA-associated ions, which leads to the swelling of vesicles, followed by fatty acid uptake and vesicle growth. According to the same article, isotonic vesicles do not

grow under the same conditions. This indicates that if the membrane of prebiotic organisms did consist of similar molecules, they had an advantage in replication over the isotonic assemblies. Such results provide clues about Darwinian evolution at very early stages.

The ability to produce minimal cells leads, and has led in the past, to beneficial practical applications mainly in the medical and pharmaceutical fields, but not exclusively there. For instance, the controlled release of the drug doxorubicin was reported during compartmentalization studies with membrane coated microgels[146]. Another example is the production and usage of artificial red blood cells for oxygen therapy [147]. A technical example is the development of biobatteries/biofuels. Xu *et al.* [148] achieved a protocell bio-battery which can convert chemical energy (energy stored in a concentration gradient) to electrical energy, using a hybrid system of natural ion channels and pumps incorporated into supported lipid membranes. One other potential benefit of protocells is cell-free protein synthesis[149]. A declared long-term goal is the development of synthetic cell culture models. Current toxicity tests on human liver cells are suitable only for short term toxicity caused by high doses, not for chronic toxicity. Moreover, with synthetic cell lines, toxicity tests could be performed in earlier stages of drug development, avoiding animal based clinical trials[150].

There are two common approaches to the creation of artificial cells. The top-down approach involves the genetic reprogramming of existing cells[15]. Starting point is a complex biological cell. By knocking out "unnecessary" genes, a minimal cell model containing a fraction of original genome is created, which is just sufficient to maintain the basic cell functions. In contrast, the bottom-up approach aims to develop a cell starting from biomimetic containers. Subsequently, the desired additional structural and functional elements are step by step constructed and assembled [139,140,143,151](**Figure 5.1**).

The bottom-up construction of a cell begins with the container, defining a semi-permeable boundary. Abundantly used in this context are vesicles or liposomes (**Figure 5.1 A**), assembled from phospholipids, which are also the main components of plasma membranes[152]. An alternative is to start from highly elastic polymerosomes, which are vesicles assembled from amphiphilic block co-polymers[151]. A few other candidates are protein, peptide or amino acid assemblies[153-155]. The next step forward is shown in (**Figure 5.1 B**).
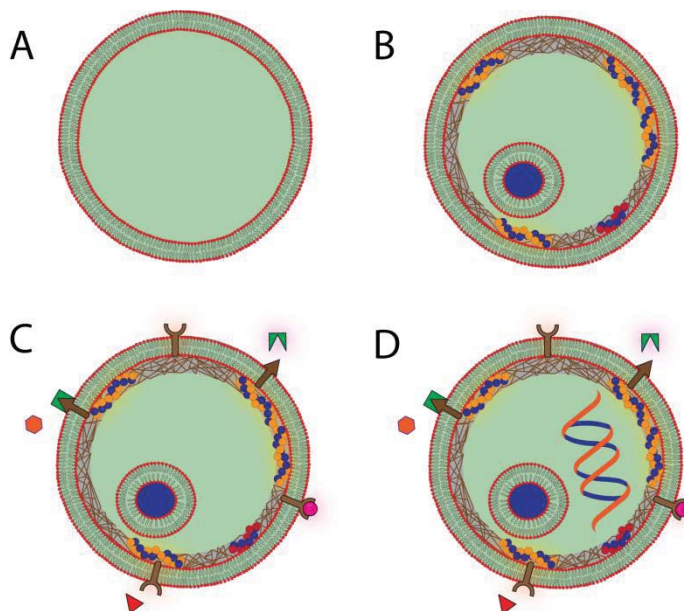
Figure 5.1 Bottom-up approach for artificial cell construction. *(A) The liposome as a biomimetic container. (B) Construction mimics: implementation of cytoskeleton components and compartmentalization. (C) Communication and exchange mimics: Signaling, intra-, and extra- cellular trafficking. (D) Cell-free metabolic processes: enzyme synthesis and replication.*

It entails the reinforcement of the container with endo- and exo-cytoskeleton elements providing shape and stability; as well as compartmentalization and motility. Cell cytoplasm contains compartments of organelles which are surrounded by a single or double bilayer membrane. Each compartment is isolated and can achieve a unique concentration of solutes, pH or enzymatic activity. This feature, referred to as compartmentation or compartmentalization, gives the cell the opportunity to perform various (potentially incompatible) metabolic activities simultaneously. One experimental strategy is to exploit phase transitions and separations of encapsulated soluble polymers in response to external stimuli. A few examples are poly-(N-isopropyl acrylamide)[156], synthetic polyelectrolytes [157] or binary PEG-dextran[158] mixtures. The third step in the bottom-up approach is about mimicking cell properties which play a role in the chemical communication of a cell with its external environment (**Figure 5.1 C**). This involves processes such as signaling, endo- and exocytosis. A successful model for artificial exocytosis of vesicles has been achieved by

means of microinjection techniques, involving the release of neurotransmitters from lipid vesicles [159-160].

The final step in constructing a minimal cell would be completed by performing enzymatic catalysis and replication (**Figure 5.1 D**). As mentioned further above, critical requirements are metabolic functions and self-reproduction. Currently there are a variety of studies reporting on cell-free transcription, translation and protein expression using biomimetic containers[11,14,161]. However, these studies have not yet been merged with other steps to accomplish a complete artificial cell model.

With my own research, I have touched a number of aspects, which I consider related to artificial cell engineering. In the following I summarize these aspects mainly related to cell-like behavior, which have been observed or experimentally established in this work.

The FGUV as a biomimetic container:

One major step in artificial cell research is the establishment of a biomimetic container. For the living cell this container is the plasma membrane, an intact, semi-permeable fluid lipid membrane, integrated with proteins and other molecules. The majority of model studies employ liposomes assembled from phospholipids as fluidic and elastic containers. The elasticity of the plasma membrane is essential, since cells can undergo shape changes which must be compensated[162]. Giant unilamellar vesicles can undergo minor shape transitions, but if the membrane is under tensile stress, they rapidly break[41]. Lipid membranes have a very low tolerance to tension (stretching). Cells overcome this problem by utilizing lipid reservoirs. Lipid droplets[16] or wrinkled fragments of the plasma membrane[17] act as lipid sources, balancing the plasma membrane tension. The FGUVs used in various parts of my work (**Figure 5.2**), add this additional aspect to liposomal biomimetic containers. The FGUVs are at all times connected to MLV reservoirs. If the tension influences the membrane, more lipids from the reservoir can be supplied to the unilamellar vesicle and the stress is balanced. Previously reported nanotube-vesicle networks were based upon a similar connection between a multilamellar vesicle and a giant unilamellar vesicle. Due to the much smaller internal volume, the FGUV system is less sensitive to osmotic stress, and has the benefit of a solid support.
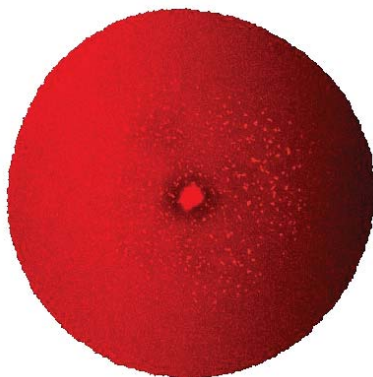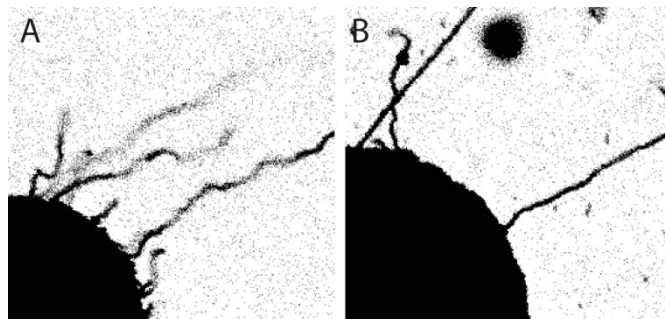
Figure 5.2. **Confocal fluorescence micrograph of a FGUV (top view)**. *The bright spot in the center of the circular double bilayer spread is the MLV. The FGUV is connected to the MLV at all times.*

Tube formation:

Caveolae which are abundant membrane invaginations particularly in muscle cells, adipocytes, and endothelial cells, have come in recent years into focus of cell mechanistic studies[162-163]. These invaginations are primarily utilized to buffer the mechanical stress in the plasma membrane in an ATP-independent manner. The caveolae formation is reversible. During stressful conditions the caveolae disappear, merging into the membrane, and when stress is released, they form again[163]. This is reminiscent of the reversible tubulation in FGUVs, observed in Paper III (**Figure 5.3**). If the membrane is under conditions of relatively low tension, the tubes form due to the spontaneous curvature induced by the nanoparticles (**Figure 5.3 A**). When adhesion to the surface is increased significantly, controlled by means of Ca^{2+} concentration, the membrane tension increases, and tubes retract (**Figure 5.3 B**). The forming and retracting tubes can be interpreted as a second lipid reservoir for the FGUV, in addition to MLVs.

The caveolae form due to the increase in spontaneous curvature in the plasma membrane, caused by a caveolar serum deprivation protein[164]. This is similar to the formation of invaginations in plasma membranes due to the adsorption of virus capsides[76]. In Paper III, we encapsulated nanoparticles in FGUVs to induce tubulation. Unlike the invaginations in cell membranes, the tubes were created outwards. This was expected since the nanoparticles were adhering to the interior of the proximal bilayer of the FGUV.

Figure 5.3. Formation and retraction of nanotubes. *Inverted confocal fluorescence micrographs of a FGUV, exhibiting tube formation and retraction. (A) Encapsulated nanoparticles inside the FGUV increase the spontaneous curvature of the membrane and facilitate the formation of nanotubes in the low tension regime. (B) Due to high membrane tension, the tubes retract, except for a few which become anchored to the surface during tubulation*.

The nanoparticles used in the study were comparable in size to the virus particles which stimulate tube formation in the plasma membranes. This similarity is of significance, since the occurrence of tubulation is sensitive to the ratio of bending energy to the particle size[76].

Pore formation and repair mechanisms:

A number of papers in this thesis (Paper IV, V and VI) focus on pores or ruptures in lipid membranes. Our observations in Paper III show resemblance to rupture repair in biological cells (**Figure 5.4**). The pore closure aspect is reminiscent of the "exocytotic reduction mechanism" for large area pores in biological cells, one of the three currently discussed cell repair mechanisms[165]. It requires that sufficient lipid material is supplied to the membrane regions surrounding the pore, and that the adhesion to the underlying support is simultaneously reduced. Ca^{2+} pinning in our system initially prevents the pore from enlarging. This corresponds well to the role of the cytoskeleton, which protects the cell membrane from further rupturing, and aids the membrane in resealing.

In Paper IV, the observation of irregular ruptures in FGUV membranes led us to examine a possible analogous response in cell membranes. Experiments performed in Chinese Hamster Ovary (CHO) cells under similar conditions led to the formation of fractal ruptures in spreading cell membranes. This
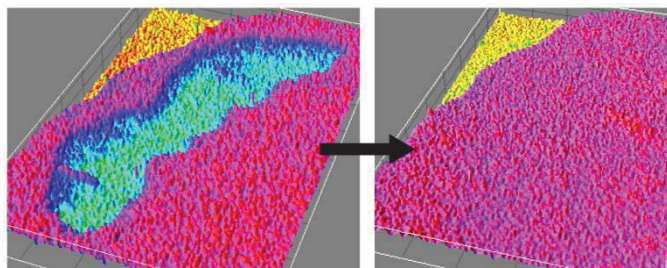
Figure 5.4. Repair of large area pores (~100 μm in length) in supported membranes. *The 3D fluorescence intensity micrographs of a large area pore in the proximal bilayer of a FGUV, which is repaired due to the pore edge tension, controlled by the removal of pinning sites at the pore edge.*

study showed that observations on FGUV can lead to the discovery of unknown behavior of cells.

Chemo-, Thermo- and Haptotaxis:

Living cells continuously probe their close-range environment and move accordingly in order to adjust to physical or chemical stimuli. Examples of such stimuli are a chemical concentration, temperature, or adhesion strength gradient. Movement in these gradients (referred to as chemotaxis, thermotaxis or haptotaxis, respectively) benefits the cells in a particular way, by improving access to nutrients, creating connectivity, evading undesirable environmental conditions or others. Cell movement is a key mechanism in the function of immune system cells, sperm cells, wound healing and cancer cell metastasis.

The molecular machinery behind cell movement is complex. It involves a cascade of signaling events, constructional elements, i.e., cytoskeleton filaments and motor proteins, as well as coordination of extreme shape dynamics of the cell. There is a variety of studies which, in vitro and without the involvement of biomimetic containers, approach the organization of the machinery involved in cell motility. A review by Schwille et al. summarizes these efforts [144]. Only a few examples employ biomimetic containers in addition to the molecular machinery to study cell movement. These include studies on encapsulated actin filaments[166], electrostatic and adhesive interactions of vesicles with an underlying bilayer [167], and some theoretical works[141-142]. The investigations leading to Paper I and Paper II have been

driven partly by the motivation to establish control over the movement of surface adhered membrane containers (giant or flat giant unilamellar vesicles) in chemical or thermal gradients, respectively.

In Paper I, using a FGUV, and Ca^{2+} as a point source of chemo-attractant, we have probed several aspects of cell migration as a response to chemical stimuli. These aspects were ligand binding, polarization of FGUV towards the chemo-attractant, and protrusion formation with high aspect ratios (**Figure 5.5**). Complementary experiments showed a reversible attractive response of suspended nanotubes towards the Ca^{2+} source. This particular finding indicates that the phenomenon is not necessarily surface dependent, but originates from the interaction of Ca^{2+} ions with the membrane.
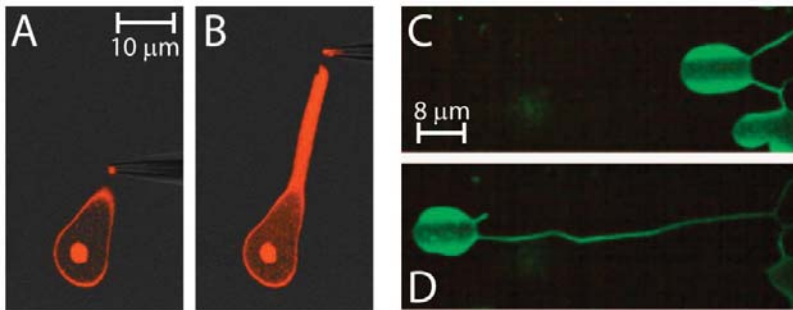
Figure 5.5 Motility of FGUVs. *(A-B) Protrusion formation in a FGUV vesicle directed by Ca^{2+} supplied via a micro injection needle. Similar protrusions are observed in cells during chemotaxis. (C-D) Artificial thermomigration of a FGUV, driven by a moving hot spot. The membrane container evades the high temperature stimulus, producing a trailing nanotube.*

Similar to chemotaxis, cells can direct their movement along temperature gradients. Temperature-directed migration of various types of cells has been established, some examples are bacteria, amoebae, *C. elegans* or sperm. The lipids in the membrane matrix of slime mold were reported to act like thermosensors, and the fluidity and re-structuring of membrane lipids were found to be effective in thermotactic behavior[168-169]. Rearrangement of the membrane lipid composition in the Paramecium cell membrane due to temperature gradients was also reported to be essential for thermotactic motion[170]. These findings indicate that lipids in the plasma membrane are involved in thermosensory transduction. However, currently, not much is

known about the molecular mechanisms and the role of lipids in thermotaxis of cells.

In cell haptotaxis, motion occurs based on selective-adhesion interactions between the cell and discrete cell matrix constituents[171]. In Paper II, we reported on a temperature gradient-defined movement of surface adhered vesicles. In our study on smooth oxide surfaces, the vesicles do not selectively control adhesion. The adhesion is rather controlled by the locally generated temperature gradient, which causes a corresponding adhesion gradient. This adhesion gradient over the surface distance covered by the FGUV causes the vesicle to migrate towards the region of high adhesion. Our study represents the first example of an experimental implementation of thermotaxis/haptotaxis of supported model membranes.

Chapter 6 : METHODS

6.1 Fluorescence and confocal laser scanning microscopy

Most of the work in this thesis involved optical microscopy to visualize the various phenomena in supported biological membranes. Both the membranes and the solid supports utilized in my experimental work are transparent to visible light, and therefore well suited for optical microscopy. The thickness of a bilayer membrane is only ~4-5 nm, which is a size range below the diffraction limit of light microscopy. Therefore direct observation is not possible. Instead, fluorescence microscopy techniques were utilized in all imaging experiments throughout my thesis work. Fluorescence microscopy requires fluorescent labeling of the bilayer, which can be conveniently achieved through incorporation of fluorophore-conjugated lipids in the membrane. Fluorophores absorb light of one wavelength (excitation) and emit it at a slightly larger wavelength within 10^{-7} to 10^{-9} s. A small portion of the excitation energy is dissipated internally, so that the emitted light is of lower energy than the incident light. If the absorbed photon introduces more energy than necessary for a simple electronic transition, the excess energy is converted into vibrational and rotational energy. **Figure 6.1** shows a simplified "Jablonski"-diagram[172], which is commonly used to represent the various absorption-emission relationships for a given molecule. Many related, and in other branches of optical microscopy and spectroscopy important aspects, such as intersystem crossing to the triplet state, internal conversion between singlet states, non-radiative relaxation, quenching and phosphorescence, are omitted in the figure for clarity.

In the different experiments two types of optical fluorescence microscopy techniques were used; laser induced fluorescence (LIF), and confocal microscopy. The experimental setup shown in **Figure 6.2** was developed in our laboratory for combined multi-wavelength LIF wide field imaging and IR laser spot heating.

Figure 6.1 Simplified Jablonski energy diagram. *A photon in the excitation light is absorbed (blue arrow) into the electronic "ground" state of a fluorophore. As a result the electronic energy is elevated to an "excited" state. The excited fluorophore releases its energy by emitting a photon (red arrow) and returns to the low energy ground state. A fraction of the absorbed light is dissipated internally (yellow arrow).*
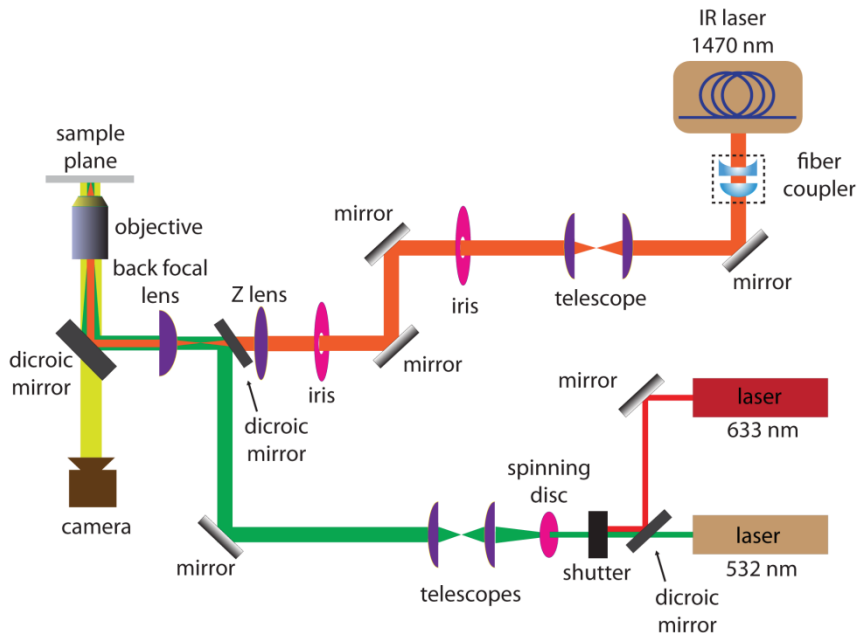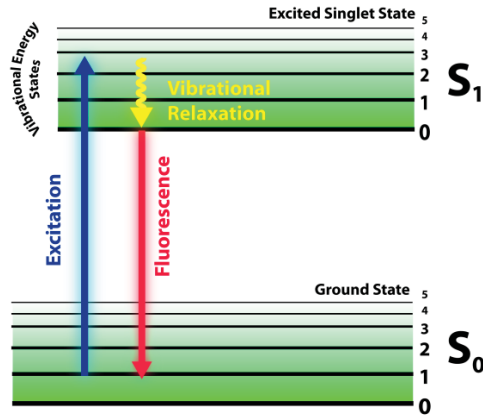
Figure 6.2 Schematic drawing of the optical setup used for laser-induced fluorescence (LIF) microscopy imaging. *The green and red lines represent the beam paths from the two diode lasers. The actual setup contains another 488 nm laser, which is omitted in the drawing. The beam paths of the 633 nm the 532 nm lasers are drawn separately until the shutter, from there on their paths are identical, and only represented by the green colored line. The orange beam path represents the additional IR laser line, utilized in the spot heating experiments.*

The system contains a commercial Leica DM-IRB differential interference contrast microscope, equipped with an in-house developed fluorescence imaging setup. It features three individual diode lasers (488 nm, 543 nm, 633 nm), and a 1470 nm diode laser, which will be described further down, as well as a high performance CCD camera for image recording. The visible laser beams pass a diffuser, which reduces the typical speckle pattern which is produced by the mutual interference of the wavefronts in the laser beam, and a mechanical shutter. Then the beams are expanded in a telescope and finally focused by the back aperture lens onto the fixed focal plane of the objective. From there it diverges and produces a homogenously illuminated field of view.

Today's high numerical aperture optics in commercial wide field microscopes achieve a resolution of 250 nm. The best resolution can be obtained with a homogeneous refractive index, high fluorescence intensity, and low background signal. An improvement is achieved by deconvolution of wide field image z-stacks, using a computational post processing to construct the most probable object depending on the "point spread function" (PSF)[173]. The PSF is determined experimentally for each optical setup. This technique removes the out-of-focus light and enhances contrast.

Confocal laser scanning microscopy further advances image quality, and can be used to render three-dimensional fluorescence images. A tightly focused laser beam scans the sample, and a pinhole aperture allows collecting light from only one focal plane, so that much of the out of-focus light is eliminated. Due to the reduction of laser light back-scattered from the surface, confocal microscopy is very suitable for thin fluorescent surface-based samples, such as biomembranes or phospholipid bilayers. A disadvantage of scanning confocal microscopy is the relatively poor time resolution. A high resolution scan takes milliseconds to seconds, which has proven to be too slow to capture, for example, the finer details of the very rapid avalanche rupture events occurring in a bilayer membrane.

6.2 Deposition of thin films

The high energy surfaces required for the FGUV spreading experiments were fabricated and characterized in the Nanofabrication Laboratory MC2 at Chalmers, a state-of-the-art cleanroom for the processing of materials required in micro- and nanoelectronics. Silicon oxide films were fabricated in the facility and instantly used in the spreading experiments. Thin films of

SiO$_2$, Al$_2$O$_3$, required for the experimental work in Papers I-VII, were created by reactive sputtering[174] of Si and Al, using oxygen as a process gas. Briefly, sputtering is the liberation of atoms from the surface of a solid "target". This is achieved in a vacuum, by showering the surface with particles of kinetic energies far higher than the common thermal energies. Atoms transferred into the gas phase by the sputtering technique are out of thermodynamic equilibrium, and tend to release energy by associating with the surfaces in the vacuum chamber. If a substrate, such as a wafer, is placed inside the chamber, it will be coated with a film of atoms originating from the sputter target. Sputtering usually uses argon plasma as source of energetic particles. If a reactive gas, for example oxygen or nitrogen, is added to a small proportion to the sputter gas, an instant chemical reaction between the sputtered atoms and the gas leads to deposition of the reaction product. In case of the above mentioned gases the deposited film is an oxide or nitride. For use in thermotaxis studies (Paper II), a different strategy was chosen to fabricate an Al$_2$O$_3$ film. First an Al film of 10 nm was deposited by sputtering and subsequently plasma-oxidized for a short period of time. This method produced surfaces of similar morphology, but of very different zeta potential, which produced adhesion conditions suitable for thermomigration of the FGUVs.

6.3 Scanning probe microscopy

Scanning Probe Microscopy (SPM), commonly known as Atomic Force Microscopy (AFM)[52,175-177], is a near field surface microscopy technique which reveals topographical information with atomic resolution. In this work, SPM was used for surface characterization. The technique neither requires any labeling, fixing, or coating of the samples, nor (strictly) high vacuum conditions during measurements. The AFM image of a surface is obtained by scanning the (nanosized) tip of a microscopic cantilever across the surface. The cantilever is deflected according to the force interactions between tip and sample, and this deflection is transduced via a laser spot reflected from the upper surface of the cantilever into an array of photodiodes. There are two main scanning modes of AFM based on tip dynamics: Static and dynamic modes. In static mode (contact mode), the cantilever tip is immobile and dragged continuously in physical contact (<0.5 nm) with the surface of the sample. A drawback of this method is the damage of the sample by the cantilever. In the dynamic mode, the cantilever tip oscillates. In the non-contact mode/frequency modulation (FM) operation, which is one of the two variations of the dynamic mode, the tip oscillates 5–40 nm

above the sample but does not touch it. Mainly attractive van der Waals forces and electrostatic (or magnetic) forces hinder the oscillation of the tip and reduce the resonance frequency. Changes in the frequency modulation provide information about the sample–tip interactions. This mode of operation is ideal for very soft/elastic samples since the attractive force between the tip and the sample is $\sim 10^{-12}$ N. Unfortunately, high atomic resolution in this mode is achieved only in high vacuum, because in ambient conditions a thin water layer covering the sample tends to attract the tip. The second dynamic mode, tapping mode, is a hybrid mode between static contact mode and non-contact dynamic mode. Other names for tapping mode are intermittent contact mode/amplitude-modulation (AM) operation. Tapping mode overcomes the adverse effect of the water layer above the sample which is experienced in non-contact mode. The tip oscillates with amplitudes of 20–100 nm (which is a much bigger amplitude in comparison with the amplitude of the noncontact mode [<5 nm]) and is intermittently in contact with the sample. The oscillation amplitude (oscillation energy) is big enough to overcome surface attraction for a wide range of vertical positions of the cantilever, while lateral forces are eliminated completely. Perturbations of the oscillation amplitude are detected as a feedback signal.

The tip dimensions also influence the resolution of the image. In Paper VI we used a standard probe with tip radius of 12 nm (TESPA probe, Bruker) in tapping mode. In Paper II a high resolution probe with a spike radius of 1 nm (High Resolution Probe, Micromash) was used, which led to greatly improved image resolution.

## 6.4 Scanning electron microscopy

Scanning Electron Microscopy (SEM) was used for surface characterization of solid supports in Paper II. Electron microscopy techniques use electrons instead of photons to obtain information from their interactions with the sample[178]. Briefly, the sample is laterally scanned with a focused beam of electrons, which is interacting with the sample and produces secondary (low-energy <50 eV) and backscattered (high energy) electrons. These electrons are projected onto a scintillator-photomultiplier detection device (Everhart-Thornley detector). SEM can provide information about the surface topography and composition of the sample with 100× greater resolution compared to optical microscopy techniques. SEM is the most efficient for conductive samples. Semi and non-conductive samples can be coated with thin conductive films to avoid charging effects[179].

6.5 Microfluidics

Paper VII and Paper VIII involve the use of microfluidic devices for the manipulation of solid supported molecular lipid films. Microfluidics[180] is the science of manipulating small volumes of liquids (10^{-9} to 10^{-18} liters) in channels of ten to a few hundred micrometers[181-182]. Microfluidic technology has capabilities which bulk chemistry cannot provide: the ability to handle very small amounts of liquids, high resolution and sensitivity in separation and detection, low consumption of sample, solvents and reagents, as well as small footprints for analytical devices. Liquids in small channels exhibit laminar flow, which offers a better control over the concentrations of molecules in space and time.

The earlier utilized glass and silicon for microfluidic chips is now frequently replaced by plastics, most widely the optically transparent soft elastomer poly-(dimethylsiloxane) (PDMS). In Paper VII and Paper VIII PDMS was the material of choice for fabricating the microfluidic device employed in the experimental work to study the self-spreading of supported lipid double bilayers: The microfluidic diluter in Paper VII provided fast and precise dilution of calcium containing buffer solution. The Ca^{2+} concentration necessary to initiate lipid spreading was determined by means of this device, which saved countless hours of preparing series of dilutions manually by exchanging buffers.

In Paper VIII we used a multifunctional pipette [183], also fabricated in PDMS, to produce and functionalize lipid films and networks in desired patterns and compositions. This innovative approach to membrane assembly by direct writing exploits the hydrodynamic confinement of a small fluid volume at the tip of a pipette-shaped microfluidic solution dispenser (**Figure 6.3 A**). The multifunctional pipette is essentially an ad-hoc microflow chamber with virtual boundaries. By means of a positive and negative pressure source, a continuously re-circulating injection volume is maintained at the tip of the device (**Figure 6.3 B and C**). This effectively superfuses any object within 5~100 μm from the pipette tip. Flow re-circulation provides a means to maintain a stationary concentration pattern which would otherwise rapidly dissipate. The extent of the re-circulation zone is controlled by device parameters (mainly channel dimensions) and by varying the outflow to inflow ratio Q, which for confinement must be lower than a critical value $Q_{critical}$.
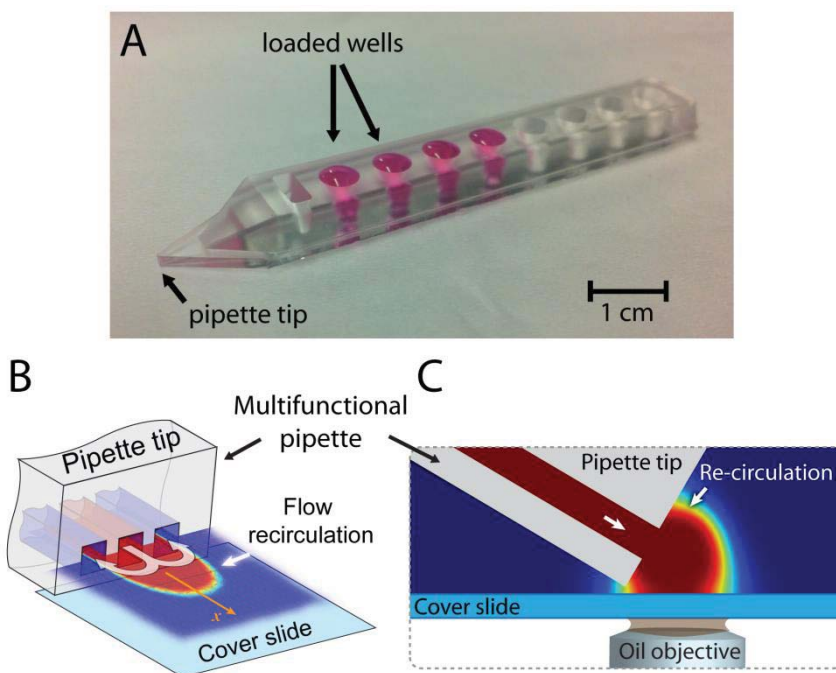
Figure 6.3 Microfluidic pipette. *(A) Photograph of the microfluidic pipette prior to its use in an experiment. The pipette consists of 8 wells. 4 of which are loaded with a fluorescently labeled lipid suspension. (B) Schematic top and side view of the re-circulation zone at the pipette tip. The color coded concentration profile, with red=highest, and blue=lowest concentration of the re-circulated compound, was obtained by a COMSOL simulation. (C) Schematic side view of the multifunctional pipette under operation conditions as used to write and manipulate bilayer membranes.*

An important aspect of the virtual re-circulation flow chamber is the fluid boundary between the open volume and the re-circulation zone. Since both are aqueous solutions, the boundary is diffusive and the width w is determined by the exchange time t, *i.e.*, the time a molecule stays in the confined volume, and the diffusivity D, so that $w \approx \sqrt{2Dt}$. The exchange time is closely related to the outflow rate Q and the volume V of the re-circulation zone. Flow rate $Q = vl^2$ and volume $V = \pi d^3/6$ define exchange time $\tau = V/Q = \pi d^3/6vl^2$, where v is the average flow velocity, l is the dimension of a square shaped channel and d is the diameter of the nearly spherical exchange volume. The experimental conditions necessary to

achieve efficient confinement, while inhibiting diffusion across the virtual boundary, are characterized by low Reynolds and high Péclet numbers.

6.6 Infrared laser technology for localized heating

Temperature represents the most important experimental variable for thermodynamic and kinetic studies of many processes in physics, chemistry and biology. Localized temperature control in microscopy experiments appears to be of considerable interest[180,184 185]. A rather convenient approach to heating is to use focused laser light in an existing microscope setup[186]. Due to the low absorption of biological samples in the near infrared (IR-A) range and below, this approach is not considered to be efficient. The long-wavelength infrared (IR-B) is a better alternative, since the absorption of biological matter (protein and water) increases significantly above 1,450 nm [187-189]. From 750 nm, the absorption of water increases over 6 orders of magnitude with an absorption maximum at 2940 nm. Diode lasers as power sources in this wavelength range are easily commercially available, as the IR-B wavelength range is used for long-distance telecommunications. For the purpose of heating a confined volume inside a buffer droplet under an inverted microscope, we have constructed an IR-B laser setup, which focuses the radiation from a 1470 nm optical fiber laser onto a microscope substrate (**Figure 6.2**). In Paper II, we used this setup as a point heater to create a heating spot of 20 micrometers in diameter in order to thermally manipulate supported membrane patches of approximately the same size.

Chapter 7 : SUMMARY & REMARKS

Paper I. Simple features reminiscent of cell migration have been achieved by applying a chemical point source. The point source was introduced by a microinjection needle loaded with Ca^{2+} ions in millimolar concentrations. In response to the stimulus, the surface adhered FGUVs polarized and formed protrusions towards the chemical stimulus. The use of negatively charged lipids resulted in the contractive behavior of vesicles, and oscillating shape dynamics according to the Ca^{2+} concentration in the vicinity of the vesicle. Similar oscillations observed in suspended nanotubes indicate a non-surface-based interaction.

Paper II. The migration of flat giant vesicles was achieved on plasma oxidized aluminum surfaces, directed by locally applied temperature gradients. The local temperature gradients were generated by surface spot heating by means of a fiber optical IR laser. The vesicles evaded the temperature increase by migrating along the gradients, leaving behind a trailing nanotube. We show for the first time experimentally the thermomigration of a fluidic mesoscale material, and present a contact-free technology for the fabrication of lipid nanotubes and FGUV-nanotube-networks.

Paper III. Semiconductor nanoparticles of virus particle-like morphology were inserted into flat giant unilamellar vesicles. The particles induced the spontaneous formation of lipid nanotubes, emerging from the flat vesicles and elongating gradually into the ambient solution. The tube formation, could be dynamically controlled by changing the Ca^{2+} concentration in the ambient buffer.

Paper IV. Two new rupture modes of model membranes have been discovered. The rupture formation was found to be analogous to patterns formed during viscous fingering in porous media. One of the modes also displays crackling noise dynamics, featuring sudden intermittent bursts over a broad size range. The observed model membrane rupture behavior was successfully recreated in cells, which in the presence of Eu^{3+} ions spread on SiO_2 and ruptured in similar patterns.

Paper V. Experimental evidence for a rapid lipid transfer mode between bilayer membranes in double bilayer stacks was reported. An analysis of bilayer ruptures observed on isolated membrane islands indicated that one single fusion or hemi-fusion-like pore is sufficient to accommodate the observed flow in the membranes. The findings indicate biological relevance with respect to transfer of molecules through double-bilayer enveloped organelles in cells.

Paper VI. Pore repair mechanisms in flat giant vesicles were studied. Ca^{2+} pinning sites, which provide pore edge stability, were chemically removed by means of chelators. The removal caused a drop in pore edge tension and led eventually the closure of large area pores of several tens of micrometers in size.

Paper VII. The Ca^{2+} ion concentration required to initiate the formation of a FGUV has been determined by means of an open-volume microfluidic diluter. The device, operating on the fluidic equivalent to pulse width modulation commonly utilized in electronics, is capable of delivering dilution series up to 100 fold with high linearity. By exposing a MLV vesicle to the diluter flow, the effective concentration of Ca^{2+} to initiate lipid spreading was determined to be 0.8 mM.

Paper VIII. The formation of supported 2D single bilayer networks was achieved by means of a microfluidic pipette. The hydrodynamically isolated recirculation at the tip of the pipette made it possible to directly write and functionalize lipid bilayer membranes onto a surface, without contaminating adjacent regions of the substrate or the ambient buffer solution. This new nanotechnological platform was coined "lab on a membrane", since it gives unprecedented control over the area coverage, film geometry and composition of solid-supported lipid bilayer membranes.

In my thesis I describe generation, characterization and use of the self-spreading double bilayer membrane. This variant of solid-supported bilayer membranes is in fact a flat giant unilamellar vesicle, which has only a fraction of the internal volume of conventional giant unilamellar vesicles. It possesses features of supported membranes, such as flatness, large area coverage and high mechanical stability, and of giant vesicles, such as the ability to encapsulate nanoparticles. I consider the FGUV to be both an

experimental platform to study various aspects of cell like behavior on intact model membranes, and a nanotechnological platform, useful for example to build mesoscale membrane architectures and networks. In the publications which emanated from my research I present concepts and applications from both the scientific and the technological point of view.

I envision several directions, in which research on FGUVs can proceed in the future. It is evident that the double bilayer nature provides the opportunity to incorporate membrane proteins. A significant benefit is the cushion effect provided by the water space and the proximal bilayer, which is reminiscent of tethered bilayers, but avoids the decrease in membrane fluidity experienced in tethered bilayer films. Incorporation of membrane proteins into FGUVs could allow the investigation of membrane protein dynamics under conditions most similar to the plasma membrane. Very much related to this concept is the desire to produce FGUVs by means other than spreading from a multilamellar reservoir. Attempts to characterize the spreading dynamics quantitatively (in terms of a relationship for the spreading coefficient) with good repeatability were so far unsuccessful, demonstrating that the spreading approach is today a rather unpredictable process, which can hardly be developed into a model membrane technology.

In contrast, if a fabrication approach equivalent to the direct writing of bilayers by means of the multifunctional pipette can be developed, the potential of the FGUV as nanotechnological concept will be unlocked. A promising direction for future research is therefore the investigation of lipid deposition techniques for the creation of supported double bilayers. The multifunctional pipette offers great conceptual flexibility in terms of spatial and compositional control over the membrane source and deposition parameters.

Research on FGUVs is truly interdisciplinary, requiring input from several scientific and engineering disciplines, most notably chemical and physical soft matter science, surface science, and microtechnology, which makes this particular research exciting and challenging at the same time.

ACKNOWLEDGEMENTS

BIBLIOGRAPHY

1   Zamir, E. & Geiger, B. Molecular complexity and dynamics of cell-matrix adhesions. *Journal of Cell Science* **114**, 3583-3590 (2001).

2   Kam, L. C. Capturing the nanoscale complexity of cellular membranes in supported lipid bilayers. *Journal of Structural Biology* **168**, 3-10, doi:10.1016/j.jsb.2009.05.006 (2009).

3   Coskun, U. & Simons, K. Cell Membranes: The Lipid Perspective. *Structure* **19**, 1543-1548, doi:10.1016/j.str.2011.10.010 (2011).

4   Van Meer, G., Voelker, D. R. & Feigenson, G. W. Membrane lipids: Where they are and how they behave. *Nature Reviews Molecular Cell Biology* **9**, 112-124 (2008).

5   Bloom, M., Evans, E. & Mouritsen, O. G. Physical properties of the fluid bilayer component of cell membranes - a perspective. *Q. Rev. Biophys.* **24**, 293-397 (1991).

6   Sackmann, E. Supported membranes: Scientific and practical applications. *Science* **271**, 43-48 (1996).

7   Mahowald, M. B. Protocell research and its implications. *Perspectives in Biology and Medicine* **53**, 136-147 (2010).

8   Walde, P. Building artificial cells and protocell models: Experimental approaches with lipid vesicles. *BioEssays* **32**, 296-303 (2010).

9   Chen, I. A. & Walde, P. From self-assembled vesicles to protocells. *Cold Spring Harbor perspectives in biology* **2** (2010).

10   Dzieciol, A. J. & Mann, S. Designs for life: Protocell models in the laboratory. *Chemical Society Reviews* **41**, 79-85 (2012).

11   Tawfik, D. S. & Griffiths, A. D. Man-made cell-like compartments for molecular evolution. *Nature Biotechnology* **16**, 652-656 (1998).

12   Kay, R. R., Langridge, P., Traynor, D. & Hoeller, O. Changing directions in the study of chemotaxis. *Nature Reviews Molecular Cell Biology* **9**, 455-463, doi:10.1038/nrm2419 (2008).

13   Lincoln, T. A. & Joyce, G. F. Self-Sustained Replication of an RNA Enzyme. *Science* **323**, 1229-1232, doi:10.1126/science.1167856 (2009).

14   Noireaux, V. & Libchaber, A. A vesicle bioreactor as a step toward an artificial cell assembly. *Proceedings of the National Academy of Sciences of the United States of America* **101**, 17669-17674 (2004).

15   Glass, J. I. *et al.* Essential genes of a minimal bacterium. *Proceedings of the National Academy of Sciences of the United States of America* **103**, 425-430 (2006).

16   Guo, Y., Cordes, K. R., Farese Jr, R. V. & Walther, T. C. Lipid droplets at a glance. *Journal of Cell Science* **122**, 749-752 (2009).

17   Hallett, M. B., Von Ruhland, C. J. & Dewitt, S. Chemotaxis and the cell surface-area problem. *Nature Reviews Molecular Cell Biology* **9**, 662 (2008).

18   DeGennes, P. G., Brochard-Wyart, F. & Quéré, D. *Capillarity and Wetting Phenomena* (Springer, 2004).

19   Cao, G. & Wang, Y. *Nanostructures and Nanomaterials Synthesis, Properties, and Applications (2nd Edition).* (World Scientific Publishing Co. Pte. Ltd., 2011).

20   Israelachvili, J. N. *Intermolecular and Surface Forces*. 3rd edn, (Elsevier, 2011).

21   Shuttleworth, R. The surface tension of solids. *Proceedings of the Physical Society of London Section A* **63**, 444-457, doi:10.1088/0370-1298/63/5/302 (1950).

22   Czolkos, I., Jesorka, A. & Orwar, O. Molecular phospholipid films on solid supports. *Soft Matter* **7**, 4562-4576 (2011).

23   De Gennes, P. G. Wetting: Statics and dynamics. *Reviews of Modern Physics* **57**, 827-863 (1985).

24   Nychka, J. A. & Gentleman, M. M. Implications of wettability in biological materials science. *JOM* **62**, 39-48 (2010).

25   Giovambattista, N., Debenedetti, P. G. & Rossky, P. J. Effect of surface polarity on water contact angle and interfacial hydration structure. *J. Phys. Chem. B* **111**, 9581-9587, doi:10.1021/jp071957s (2007).

26   Wenzel, R. N. Resistance of solid surfaces to wetting by water. *Industrial and Engineering Chemistry* **28**, 988-994, doi:10.1021/ie50320a024 (1936).

27   Cassie, A. B. D. & Baxter, S. Wettability of porous surfaces. *Transactions of the Faraday Society* **40**, 0546-0550, doi:10.1039/tf9444000546 (1944).

28   Crick, C. R. & Parkin, I. P. Preparation and characterisation of super-hydrophobic surfaces. *Chemistry - A European Journal* **16**, 3568-3588 (2010).

29   Solga, A., Cerman, Z., Striffler, B. F., Spaeth, M. & Barthlott, W. The dream of staying clean: Lotus and biomimetic surfaces. *Bioinspiration and Biomimetics* **2**, S126-S134 (2007).

30   Nissen, J., Jacobs, K. & Rädler, J. O. Interface dynamics of lipid membrane spreading on solid surfaces. *Physical Review Letters* **86**, 1904-1907 (2001).

31   Rädler, J., Strey, H. & Sackmann, E. Phenomenology and kinetics of lipid bilayer spreading on hydrophilic surfaces. *Langmuir* **11**, 4539-4548 (1995).

32   Nissen, J., Gritsch, S., Wiegand, G. & Rädler, J. O. Wetting of phospholipid membranes on hydrophilic surfaces - Concepts towards self-healing membranes. *European Physical Journal B* **10**, 335-344 (1999).

33   Fahy, E. *et al.* A comprehensive classification system for lipids. *Journal of Lipid Research* **46**, 839-861 (2005).

34   Shevchenko, A. & Simons, K. Lipidomics: Coming to grips with lipid diversity. *Nature Reviews Molecular Cell Biology* **11**, 593-598 (2010).

35   Brown, H. A. & Murphy, R. C. Working towards an exegesis for lipids in biology. *Nature Chemical Biology* **5**, 602-606, doi:10.1038/nchembio0909-602 (2009).

36   Quehenberger, O. *et al.* Lipidomics reveals a remarkable diversity of lipids in human plasma1. *Journal of Lipid Research* **51**, 3299-3305 (2010).

37   Dowhan, W. Vol. 66 *Annual Reviews of Biochemistry* 199-232 (1997).

38   Wenk, M. R. The emerging field of lipidomics. *Nature Reviews Drug Discovery* **4**, 594-610 (2005).

39   Van Echten-Deckert, G. & Walter, J. Sphingolipids: Critical players in Alzheimer's disease. *Progress in Lipid Research* **51**, 378-393 (2012).

40   Helfrich, W. Elastic properties of lipid bilayers: theory and possible experiments. *Zeitschrift fur Naturforschung. Teil C: Biochemie, Biophysik, Biologie, Virologie* **28**, 693-703 (1973).

41   Rawicz, W., Olbrich, K. C., McIntosh, T., Needham, D. & Evans, E. Effect of chain length and unsaturation on elasticity of lipid bilayers. *Biophysical Journal* **79**, 328-339 (2000).

42   Hanson, D. E. & Martin, R. L. How far can a rubber molecule stretch before breaking? Ab initio study of tensile elasticity and failure in single-molecule polyisoprene and polybutadiene. *Journal of Chemical Physics* **130** (2009).

43   Antonietti, M. & Förster, S. Vesicles and Liposomes: A Self-Assembly Principle Beyond Lipids. *Advanced Materials* **15**, 1323-1333 (2003).

44   Karatekin, E. *et al.* Cascades of transient pores in giant vesicles: Line tension and transport. *Biophysical Journal* **84**, 1734-1749 (2003).

45   Zhelev, D. V. & Needham, D. Tension-stabilized pores in giant vesicles: Determination of pore size and pore line tension. *Biochimica et Biophysica Acta - Biomembranes* **1147**, 89-104 (1993).

46   Marrink, S. J. & Mark, A. E. Molecular Dynamics Simulation of the Formation, Structure, and Dynamics of Small Phospholipid Vesicles. *Journal of the American Chemical Society* **125**, 15233-15242 (2003).

47   Hu, M., Briguglio, J. J. & Deserno, M. Determining the Gaussian curvature modulus of lipid membranes in simulations. *Biophysical Journal* **102**, 1403-1410 (2012).

48   Seddon, J. M. & Templer, R. H. in *Handbook of Biological Physics* Vol. 1   Ch. 3, 97-160 (Elseiver, 1995).

49   Boal, D. *Mechanics of Cell*. (Cambridge University Press, 2002).

50   Cullis, P. R., Hope, M. J. & Tilcock, C. P. S. Lipid polymorphism and the roles of lipids in membranes. *Chemistry and Physics of Lipids* **40**, 127-144 (1986).

51   Longley, W. & McIntosh, T. J. A bicontinuous tetrahedral structure in a liquid-crystalline lipid. *Nature* **303**, 612-614 (1983).

52   Gözen, I. & Jesorka, A. Instrumental methods to characterize molecular phospholipid films on solid supports. *Analytical Chemistry* **84**, 822-838 (2012).

53   Rossi, C. & Chopineau, J. Biomimetic tethered lipid membranes designed for membrane-protein interaction studies. *European Biophysics Journal* **36**, 955-965 (2007).

54   Naumann, R. L. C., Nowak, C. & Knoll, W. Proteins in biomimetic membranes: Promises and facts. *Soft Matter* **7**, 9535-9548 (2011).

55   McCullough Iii, D. H. & Regen, S. L. Don't forget Langmuir-Blodgett films. *Chemical Communications*, 2787-2791 (2004).

56   Charitat, T., Bellet-Amalric, E., Fragneto, G. & Graner, F. Adsorbed and free lipid bilayers at the solid-liquid interface. *European Physical Journal B* **8**, 583-593 (1999).

57   Reviakine, I. & Brisson, A. Formation of supported phospholipid bilayers from unilamellar vesicles investigated by atomic force microscopy. *Langmuir* **16**, 1806-1815 (2000).

58   Leng, J., Nallet, F. & Roux, D. Swelling kinetics of a compressed lamellar phase. *European Physical Journal E* **4**, 77-83 (2001).

59   Lobovkina, T. *et al.* Protrusive growth and periodic contractile motion in surface-adhered vesicles induced by Ca 2+-gradients. *Soft Matter* **6**, 268-272 (2010).

60   Dommersnes, P. G., Orwar, O., Brochard-Wyart, F. & Joanny, J. F. Marangoni transport in lipid nanotubes. *Europhysics Letters* **70**, 271-277 (2005).

61   Reboiras, M. D. Activity coefficients of CaCl2 and MgCl2 in the presence of dipalmitoylphosphatidylcholine-phosphatidylinositol vesicles in aqueous media. *Bioelectrochemistry and Bioenergetics* **39**, 101-108 (1996).

62   Akashi, K. I., Miyata, H., Itoh, H. & Kinosita Jr, K. Formation of giant liposomes promotedby divalent cations: Critical role of electrostatic repulsion. *Biophysical Journal* **74**, 2973-2982 (1998).

63   Kunze, A., Svedhem, S. & Kasemo, B. Lipid transfer between charged supported lipid bilayers and oppositely charged vesicles. *Langmuir* **25**, 5146-5158 (2009).

64   Shillcock, J. C. & Lipowsky, R. Tension-induced fusion of bilayer membranes and vesicles. *Nature Materials* **4**, 225-228 (2005).

65   Müller, M., Katsov, K. & Schick, M. A new mechanism of model membrane fusion determined from Monte Carlo simulation. *Biophysical Journal* **85**, 1611-1623 (2003).

66   Soubiran, L., Coulon, C., Sierro, P. & Roux, D. Conductivity and dielectric measurements of a lyotropic lamellar phase under shear flow. *Europhysics Letters* **31**, 243-248, doi:10.1209/0295-5075/31/4/010 (1995).

67   Michalet, X., Bensimon, D. & Fourcade, B. Fluctuating vesicles of nonspherical topology. *Physical Review Letters* **72**, 168-171 (1994).

68   Chernomordik, L. V. & Kozlov, M. M. Protein-lipid interplay in fusion and fission of biological membranes. *Annual Review of Biochemistry* **72**, 175-207 (2003).

69   Strey, R., Jahn, W., Porte, G. & Bassereau, P. Freeze fracture electron microscopy of dilute lamellar and anomalous isotropic (L3) phases. *Langmuir* **6**, 1635-1639 (1990).

70   Evans, E. & Sackmann, E. Translational and rotational drag coefficients for a disc moving in a liquid membrane associated with a rigid substrate. *Journal of Fluid Mechanics* **194**, 553-561 (1988).

71   Evans, E. A. & Hochmuth, R. M. Membrane viscoelasticity. *Biophysical Journal* **16**, 1-11 (1976).

72   Sandre, O., Moreaux, L. & Brochard-Wyart, F. Dynamics of transient pores in stretched vesicles. *Proceedings of the National Academy of Sciences of the United States of America* **96**, 10591-10596 (1999).

73   Shkulipa, S. A., Den Otter, W. K. & Briels, W. J. Thermal undulations of lipid bilayers relax by intermonolayer friction at submicrometer length scales. *Physical Review Letters* **96** (2006).

74   Czolkos, I., Erkan, Y., Dommersnes, P., Jesorka, A. & Orwar, O. Controlled formation and mixing of two-dimensional fluids. *Nano Letters* **7**, 1980-1984 (2007).

75   Davis, D. M. & Sowinski, S. Membrane nanotubes: Dynamic long-distance connections between animal cells. *Nature Reviews Molecular Cell Biology* **9**, 431-436 (2008).

76   Ewers, H. *et al.* GM1 structure determines SV40-induced membrane invagination and infection. *Nature Cell Biology* **12**, 11-18 (2010).

77   Šarić, A. & Cacciuto, A. Mechanism of membrane tube formation induced by adhesive nanocomponents. *Physical Review Letters* **109** (2012).

78   Derényi, I., Jülicher, F. & Prost, J. Formation and interaction of membrane tubes. *Physical Review Letters* **88**, 2381011-2381014 (2002).

79   McNeil, P. L. & Steinhardt, R. A. PLasma Membrane Disruption: Repair, Prevention, Adaptation. *Annual Review of Cell and Developmental Biology* **19**, 697-731 (2003).

80   Miyake, K. & McNeil, P. L. Mechanical injury and repair of cells. *Critical care medicine* **31**, S496-501 (2003).

81   Steinhardt, R. A. Cardiology: Rips repaired. *Nature* **436**, 925 (2005).

82   Yasuda, S. *et al.* Dystrophic heart failure blocked by membrane sealant poloxamer. *Nature* **436**, 1025-1029 (2005).

83   Sun, L. *et al.* The use of cationic microbubbles to improve ultrasound-targeted gene delivery to the ischemic myocardium. *Biomaterials* **34**, 2107-2116 (2013).

84   Puras, G. *et al.* Oligochitosan polyplexes as carriers for retinal gene delivery. *European Journal of Pharmaceutical Sciences* **48**, 323-331 (2012).

85   D'Acunto, M. Nanovectors for drug delivery: Long-lived pore dynamics for swelling liposomes. *Mechanics Research Communications* **38**, 34-37 (2011).

86   Schroeder, A., Kost, J. & Barenholz, Y. Ultrasound, liposomes, and drug delivery: principles for using ultrasound to control the release of drugs from liposomes. *Chemistry and Physics of Lipids* **162**, 1-16 (2009).

87   Ledley, F. D. Nonviral gene therapy: The promise of genes as pharmaceutical products. *Human Gene Therapy* **6**, 1129-1144 (1995).

88   Saitoh, A., Takiguchi, K., Tanaka, Y. & Hotani, H. Opening-up of liposomal membranes by talin. *Proceedings of the National Academy of Sciences of the United States of America* **95**, 1026-1031 (1998).

89   Remy, J. S., Kichler, A., Mordvinov, V., Schuber, F. & Behr, J. P. Targeted gene transfer into hepatoma cells with lipopolyamine-condensed DNA particles presenting galactose ligands: A stage toward artificial viruses. *Proceedings of the National Academy of Sciences of the United States of America* **92**, 1744-1748 (1995).

90   Levin, Y. & Idiart, M. A. Pore dynamics of osmotically stressed vesicles. *Physica A: Statistical Mechanics and its Applications* **331**, 571-578 (2004).

91   Guedeau-Boudeville, M. A., Jullien, L. & Di Meglio, J. M. Drug delivery: Piercing vesicles by their adsorption onto a porous medium. *Proceedings of the National Academy of Sciences of the United States of America* **92**, 9590-9592 (1995).

92   Gözen, I. *et al.* Fractal avalanche ruptures in biological membranes. *Nature Materials* **9**, 908-912 (2010).

93   Chen, C., Smye, S. W., Robinson, M. P. & Evans, J. A. Membrane electroporation theories: A review. *Medical and Biological Engineering and Computing* **44**, 5-14 (2006).

94   Shillcock, J. C. & Seifert, U. Thermally induced proliferation of pores in a model fluid membrane. *Biophysical Journal* **74**, 1754-1766 (1998).

95   Homsy, G. M. Viscous Fingering in Porous Media. *Annual Review of Fluid Mechanics* **19**, 271-311 (1987).

96   Sarma, H. K., Maini, B. B. & Jha, K. Evaluation of emulsified solvent flooding for heavy oil recovery. *Journal of Canadian Petroleum Technology* **37**, 55-62 (1998).

97   Jha, B., Cueto-Felgueroso, L. & Juanes, R. Fluid mixing from viscous fingering. *Physical Review Letters* **106** (2011).

98   Abbas, F. & Rose, D. A. Viscous fingering and gravity segregation through porous media: Experimental findings. *Earth Interactions* **14** (2010).

99   Mather, W., Mondragón-Palomino, O., Danino, T., Hasty, J. & Tsimring, L. S. Streaming instability in growing cell populations. *Physical Review Letters* **104** (2010).

100   Callan-Jones, A. C., Joanny, J. F. & Prost, J. Viscous-fingering-like instability of cell fragments. *Physical Review Letters* **100** (2008).

101   Sandnes, B., Flekkøy, E. G., Knudsen, H. A., Måløy, K. J. & See, H. Patterns and flow in frictional fluid dynamics. *Nature Communications* **2** (2011).

102   Tóth-Katona, T. & Buka, Á. Nematic-liquid-crystal-air interface in a radial Hele-Shaw cell: Electric field effects. *Physical Review E - Statistical, Nonlinear, and Soft Matter Physics* **67**, 417171-417177 (2003).

103   Løvoll, G., Méheust, Y., Toussaint, R., Schmittbuhl, J. & Måløy, K. J. Growth activity during fingering in a porous Hele-Shaw cell. *Physical Review E - Statistical, Nonlinear, and Soft Matter Physics* **70**, 026301-026301-026301-026312 (2004).

104   Saffman, P. G. & Taylor, G. The penetration of a fluid into a porous medium or Hele-Shaw cell containing a more viscous liquid. *Proceedings of the Royal Society of London Series a-Mathematical and Physical Sciences* **245**, 312-&, doi:10.1098/rspa.1958.0085 (1958).

105   Meakin, P. *et al.* Invasion percolation and secondary migration: Experiments and simulations. *Marine and Petroleum Geology* **17**, 777-795 (2000).

106   Fast, P. & Shelley, M. J. A moving overset grid method for interface dynamics applied to non-Newtonian Hele-Shaw flow. *Journal of Computational Physics* **195**, 117-142 (2004).

107   Toussaint, R., Løvoll, G., Méheust, Y., Måløy, K. J. & Schmittbuhl, J. Influence of pore-scale disorder on viscous fingering during drainage. *Europhysics Letters* **71**, 583-589 (2005).

108   Måloy, K. J., Furuberg, L., Feder, J. & Jossang, T. Dynamics of slow drainage in porous media. *Physical Review Letters* **68**, 2161-2164 (1992).

109   Roiter, Y. *et al.* Interaction of nanoparticles with lipid membrane. *Nano Letters* **8**, 941-944 (2008).

110   Sharon, E., Moore, M. G., McCormick, W. D. & Swinney, H. L. Coarsening of fractal viscous fingering patterns. *Physical Review Letters* **91**, 205504/205501-205504/205504 (2003).

111   Davidovitch, B., Levermann, A. & Procaccia, I. Convergent calculation of the asymptotic dimension of diffusion limited aggregates: Scaling and renormalization of small clusters. *Physical Review E - Statistical Physics, Plasmas, Fluids, and Related Interdisciplinary Topics* **62**, R5919-R5922 (2000).

112   Mandelbrot, B. *The fractal geometry of nature*. 3 edn, (Freeman and company, 1983).

113   Castrejón-Pita, A. A., Sarmiento-Galán, A., Castrejón-Pita, J. R. & Castrejón-García, R. Fractal Dimension in Butterflies' Wings: A novel approach to understanding wing patterns? *Journal of Mathematical Biology* **50**, 584-594 (2005).

114   Glenny, R. W. Emergence of matched airway and vascular trees from fractal rules. *Journal of Applied Physiology* **110**, 1119-1129 (2011).

115   Obert, M., Pfeifer, P. & Sernetz, M. Microbial growth patterns described by fractal geometry. *Journal of Bacteriology* **172**, 1180-1185 (1990).

116   Wang, W. & Chau, Y. Self-assembled peptide nanorods as building blocks of fractal patterns. *Soft Matter* **5**, 4893-4898 (2009).

117   Bancaud, A., Lavelle, C., Huet, S. & Ellenberg, J. A fractal model for nuclear organization: Current evidence and biological implications. *Nucleic Acids Research* **40**, 8783-8792 (2012).

118   Lieberman-Aiden, E. *et al.* Comprehensive mapping of long-range interactions reveals folding principles of the human genome. *Science* **326**, 289-293 (2009).

119   Sabín, J., Prieto, G., Ruso, J. M. & Sarmiento, F. Fractal aggregates induced by liposome-liposome interaction in the presence of Ca 2+. *European Physical Journal E* **24**, 201-210 (2007).

120   Sarangi, N. K. & Patnaik, A. Structure-directing L-tryptophan for supported DPPC helices and fractals: An alkyl-chain tilt-angle dependence. *ChemPlusChem* **77**, 898-907 (2012).

121   Moran-Mirabal, J. M., Aubrecht, D. M. & Craighead, H. G. Phase separation and fractal domain formation in phospholipid/diacetylene- supported lipid bilayers. *Langmuir* **23**, 10661-10671 (2007).

122   Glenny, R., Bernard, S., Neradilek, B. & Polissar, N. Quantifying the genetic influence on mammalian vascular tree structure. *Proceedings of the National Academy of Sciences of the United States of America* **104**, 6858-6863 (2007).

123   West, G. B., Brown, J. H. & Enquist, B. J. The fourth dimension of life: Fractal geometry and allometric scaling of organisms. *Science* **284**, 1677-1679 (1999).

124   Thamrin, C., Stern, G. & Frey, U. Fractals for physicians. *Paediatric Respiratory Reviews* **11**, 134 (2010).

125   Thakre, T., Mamtani, M., Ujaoney, S. & Kulkarni, H. Fractal dimension of the sleep state waveform in obstructive sleep apnea. *Somnologie* **15**, 249-256 (2011).

126   Paramanathan, P. & Uthayakumar, R. Fractal interpolation on the Koch Curve. *Computers and Mathematics with Applications* **59**, 3229-3233 (2010).

127   Klinkenberg, B. A review of methods used to determine the fractal dimension of linear features. *Mathematical Geology* **26**, 23-46 (1994).

128   Lovejoy, S., Schertzer, D. & Tsonis, A. A. Functional box-counting and multiple elliptical dimensions in rain. *Science* **235**, 1036-1038 (1987).

129   Li, J., Du, Q. & Sun, C. An improved box-counting method for image fractal dimension estimation. *Pattern Recognition* **42**, 2460-2469 (2009).

130   Murdzek, R. The box-counting method in the large scale structure of the universe. *Rom. J. Phys.* **52**, 149-154 (2007).

131   Sethna, J. P., Dahmen, K. A. & Myers, C. R. Crackling noise. *Nature* **410**, 242-250 (2001).

132   Niccolini, G., Durin, G., Carpinteri, A., Lacidogna, G. & Manuello, A. Crackling noise and universality in fracture systems. *Journal of Statistical Mechanics: Theory and Experiment* **2009** (2009).

133   Salje, E. K. H. *et al.* Failure mechanism in porous materials under compression: Crackling noise in mesoporous SiO2. *Philosophical Magazine Letters* **91**, 554-560 (2011).

134   Kumar, J., De, R. & Ananthakrishna, G. Intermittent peel front dynamics and the crackling noise in an adhesive tape. *Physical Review E - Statistical, Nonlinear, and Soft Matter Physics* **78** (2008).

135   Gutenberg, B. R., C. F. . *Seismicity of the Earth and Associated Phenomenona*. 2 edn, (Princeton University Press, 1949).

136   Chang, T. M. S. Semipermeable microcapsules. *Science* **146**, 524-525 (1964).

137   Andrianantoandro, E., Basu, S., Karig, D. K. & Weiss, R. Synthetic biology: New engineering rules for an emerging discipline. *Molecular Systems Biology* **2** (2006).

138   Deamer, D. A giant step towards artificial life? *Trends in Biotechnology* **23**, 336-338, doi:10.1016/j.tibtech.2005.05.008 (2005).

139   Hammer, D. A. & Kamat, N. P. Towards an artificial cell. *FEBS Letters* **586**, 2882-2890 (2012).

140   Kamat, N. P., Katz, J. S. & Hammer, D. A. Engineering polymersome protocells. *Journal of Physical Chemistry Letters* **2**, 1612-1623 (2011).

141   Melkikh, A. V. & Chesnokova, O. I. Origin of the Directed Movement of Protocells in the Early Stages of the Evolution of Life. *Origins of Life and Evolution of Biospheres*, 1-15 (2012).

142   Suzuki, K. & Ikegami, T. Shapes and self-movement in protocell systems. *Artificial Life* **15**, 59-70 (2009).

143   Murtas, G. Artificial assembly of a minimal cell. *Molecular BioSystems* **5**, 1292-1297 (2009).

144   Schwille, P. & Diez, S. Synthetic biology of minimal systems synthetic biology of minimal systems P. Schwille and S. Diez. *Critical Reviews in Biochemistry and Molecular Biology* **44**, 223-242 (2009).

145   Chen, I. A., Roberts, R. W. & Szostak, J. W. The emergence of competition between model protocells. *Science* **305**, 1474-1476 (2004).

146   Kiser, P. F., Wilson, G. & Needham, D. A synthetic mimic of the secretory granule for drug delivery. *Nature* **394**, 459-462 (1998).

147   Chang, T. M. S. From artificial red blood cells, oxygen carriers, and oxygen therapeutics to artificial cells, nanomedicine, and beyond. *Artificial Cells, Blood Substitutes, and Biotechnology* **40**, 197-199 (2012).

148   Xu, J., Vanderlick, T. K. & Lavan, D. A. Energy conversion in protocells with natural nanoconductors. *International Journal of Photoenergy* **2012** (2012).

149   Caschera, F. *et al.* Coping with complexity: Machine learning optimization of cell-free protein synthesis. *Biotechnology and Bioengineering* **108**, 2218-2228 (2011).

150   Schmidt, M. & Pei, L. Synthetic toxicology: Where engineering meets biology and toxicology. *Toxicological Sciences* **120**, S204-S224 (2011).

151   Brizard, A. M. & Van Esch, J. H. Self-assembly approaches for the construction of cell architecture mimics. *Soft Matter* **5**, 1320-1327 (2009).

152   Matosevic, S. Synthesizing artificial cells from giant unilamellar vesicles: State-of-the art in the development of microfluidic technology. *BioEssays* **34**, 992-1001 (2012).

153   Holowka, E. P. & Deming, T. J. Synthesis and crosslinking of L-DOPA containing polypeptide vesicles. *Macromolecular Bioscience* **10**, 496-502 (2010).

154   Bellomo, E. G., Wyrsta, M. D., Pakstis, L., Pochan, D. J. & Deming, T. J. Stimuli-responsive polypeptide vesicles by conformation-specific assembly. *Nature Materials* **3**, 244-248 (2004).

155   Rodríguez-Hernández, J., Babin, J., Zappone, B. & Lecommandoux, S. Preparation of shell cross-linked nano-objects from hybrid-peptide block copolymers. *Biomacromolecules* **6**, 2213-2220 (2005).

156   Węgrzyn, I. *et al.* Membrane protrusion coarsening and nanotubulation within giant unilamellar vesicles. *Journal of the American Chemical Society* **133**, 18046-18049 (2011).

157   Jesorka, A., Markström, M., Karlsson, M. & Orwar, O. Controlled hydrogel formation in the internal compartment of giant unilamellar vesicles. *J. Phys. Chem. B* **109**, 14759-14763 (2005).

158   Long, M. S., Jones, C. D., Helfrich, M. R., Mangeney-Slavin, L. K. & Keating, C. D. Dynamic microcompartmentation in synthetic cells. *Proceedings of the National Academy of Sciences of the United States of America* **102**, 5920-5925 (2005).

159   Simonsson, L., Kurczy, M. E., Trouillon, R. L., Hook, F. & Cans, A. S. A functioning artificial secretory cell. *Scientific Reports* **2** (2012).

160   Cans, A. S. *et al.* Artificial cells: Unique insights into exocytosis using liposomes and lipid nanotubes. *Proceedings of the National Academy of Sciences of the United States of America* **100**, 400-404 (2003).

161   Ota, S., Yoshizawa, S. & Takeuchi, S. Microfluidic formation of monodisperse, cell-sized, and unilamellar vesicles. *Angewandte Chemie - International Edition* **48**, 6533-6537 (2009).

162   Diz-Muñoz, A., Fletcher, D. A. & Weiner, O. D. Use the force: membrane tension as an organizer of cell shape and motility. *Trends in Cell Biology* (2012).

163   Sinha, B. *et al.* Cells respond to mechanical stress by rapid disassembly of caveolae. *Cell* **144**, 402-413 (2011).

164   Hansen, C. G., Bright, N. A., Howard, G. & Nichols, B. J. SDPR induces membrane curvature and functions in the formation of caveolae. *Nature Cell Biology* **11**, 807-814 (2009).

165   McNeil, P. L. & Terasaki, M. Coping with the inevitable: How cells repair a torn surface membrane. *Nature Cell Biology* **3**, E124-E129 (2001).

166   Miyata, H., Nishiyama, S., Akashi, K. & Kinosita, K. Protrusive growth from giant liposomes driven by actin polymerization. *Proceedings of the National Academy of Sciences of the United States of America* **96**, 2048-2053, doi:10.1073/pnas.96.5.2048 (1999).

167   Solon, J., Streicher, P., Richter, R., Brochard-Wyart, F. & Bassereau, P. Vesicles surfing on a lipid bilayer: Self-induced haptotactic motion. *Proceedings of the National Academy of Sciences of the United States of America* **103**, 12382-12387 (2006).

168   Poff, K. L. & Skokut, M. Thermotaxis by pseudoplasmodia of Dictyostelium discoideum. *Proceedings of the National Academy of Sciences of the United States of America* **74**, 2007-2010 (1977).

169   Fontana, D. R., Poff, K. L. & Haug, A. Role of bulk lipid fluidity in the thermal adaptation of Dictyostelium discoideum thermotaxis. *Experimental Mycology* **7**, 278-282 (1983).

170   Hennessey, T. M. & Nelson, D. L. Biochemical studies of the excitable membrane of Paramecium tetraurelia. VIII. Temperature-

induced changes in lipid composition and in thermal avoidance behavior. *BBA - Biomembranes* **728**, 145-158 (1983).

171   Kim, H. D. & Peyton, S. R. Bio-inspired materials for parsing matrix physicochemical control of cell migration: A Review. *Integrative Biology* **4**, 37-52 (2012).

172   Lakowicz, J. R. *Principles of Fluorescence Spectroscopy*. 3rd edn, (Springer, 2006).

173   Shaw, P. J. & Rawlins, D. J. The point-spread function of a confocal microscope: Its measurement and use in deconvolution of 3-D data. *Journal of Microscopy* **163**, 151-165 (1991).

174   Madou, M. *Fundamentals of Microfabrication*. 3 edn, (CRC Press, 2011).

175   Lucas, M. & Riedo, E. Invited review article: Combining scanning probe microscopy with optical spectroscopy for applications in biology and materials science. *Review of Scientific Instruments* **83** (2012).

176   Magonov, S. N. & Reneker, D. H. Characterization of polymer surfaces with atomic force microscopy. *Annu. Rev. Mater. Sci.* **27**, 175-222, doi:10.1146/annurev.matsci.27.1.175 (1997).

177   Carvalho, F. A. & Santos, N. C. Atomic force microscopy-based force spectroscopy - Biological and biomedical applications. *IUBMB Life* **64**, 465-472 (2012).

178   Torres, E. A. & Ramírez, A. J. In situ scanning electron microscopy. *Science and Technology of Welding and Joining* **16**, 68-78 (2011).

179   Kim, K. H., Akase, Z., Suzuki, T. & Shindo, D. Charging Effects on SEM/SIM Contrast of Metal/Insulator System in Various Metallic Coating Conditions. *Materials Transactions* **51**, 1080-1083, doi:10.2320/matertrans.M2010034 (2010).

180   Baker, M. A. B., Inoue, Y., Takeda, K., Ishijima, A. & Berry, R. M. Two methods of temperature control for single-molecule measurements. *European Biophysics Journal* **40**, 651-660 (2011).

181   Whitesides, G. M. The origins and the future of microfluidics. *Nature* **442**, 368-373 (2006).

182   Tabeling, P. *Introduction to Microfluidics*. (Oxford University Press, 2005).

183   Ainla, A., Jeffries, G. D. M., Brune, R., Orwar, O. & Jesorka, A. A multifunctional pipette. *Lab on a Chip - Miniaturisation for Chemistry and Biology* **12**, 1255-1261 (2012).

184   Kato, H., Nishizaka, T., Iga, T., Kinosita Jr, K. & Ishiwata, S. Imaging of thermal activation of actomyosin motors. *Proceedings of the National Academy of Sciences of the United States of America* **96**, 9602-9606 (1999).

185   Velve Casquillas, G. *et al.* Fast microfluidic temperature control for high resolution live cell imaging. *Lab on a Chip - Miniaturisation for Chemistry and Biology* **11**, 484-489 (2011).

186   Halloran, M. C. *et al.* Laser-induced gene expression in specific cells of transgenic zebrafish. *Development* **127**, 1953-1960 (2000).

187   Kamei, Y. *et al.* Infrared laser-mediated gene induction in targeted single cells in vivo. *Nature Methods* **6**, 79-81 (2009).

188   Liu, Y. *et al.* Evidence for localized cell heating induced by infrared optical tweezers. *Biophysical Journal* **68**, 2137-2144 (1995).

189   Ichikawa, M., Ichikawa, H., Yoshikawa, K. & Kimura, Y. Extension of a DNA molecule by local heating with a laser. *Physical Review Letters* **99** (2007).